Physics – Uspekhi **58** (10) 1002 – 1028 (2015)

CONFERENCES AND SYMPOSIA

PACS numbers: 75.30.Ds, **85.70. – w**, **85.75. – d**

Magnonics: a new research area in spintronics and spin wave electronics

S A Nikitov, D V Kalyabin, I V Lisenkov, A N Slavin, Yu N Barabanenkov, S A Osokin, A V Sadovnikov, E N Beginin, M A Morozova, Yu P Sharaevsky, Yu A Filimonov, Yu V Khivintsev, S L Vysotsky, V K Sakharov, E S Pavlov

DOI: 10.3367/UFNe.0185.201510m.1099

Contents

1. Introduction **1003**

2. Experimental and theoretical methods for studying wave processes **1003**

2.1 Mandelshtam–Brillouin spectroscopy for studying magnetic structures; 2.2 Theoretical methods

3. Application of magnetic structures in signal processing and communication systems **1007**

3.1 Distributed periodic systems; 3.2 Lumped systems (resonators); 3.3 Irregular waveguide systems; 3.4 Coupled waveguide systems; 3.5 Controllable magnetic structures

4. Existing devices and promising applications **1024**

5. Conclusions **1025**

References **1026**

Abstract. Recent results in magnonics — a topical and rapidly developing branch of spintronics and magnetoelectronics — are presented. The paper describes measurement techniques and theoretical approaches used to explore physical processes associated with the spin-wave propagation in complex nano- and micro-dimensional magnetic structures. The results of the application of magnetic structures in signal processing and transmission systems are discussed. In particular, results on spin wave propagation in distributed magnetic periodic structures, lumped systems, coupled waveguide structures, and controllable magnonic structures are considered. Specific examples of circuitry based on magnonic structures are discussed, and possibilities for further developing this circuitry are explored.

Keywords: magnonics, spintronics, spin wave electronics, magnonic crystals, microwave electronics, magnetic structures, spin waves, waveguides, magnetic films, magnonic logic, data processing devices

S A Nikitov Kotel'nikov Institute of Radio Engineering and Electronics, Russian Academy of Sciences,
ul. Mokhovaya 11-7, 125009 Moscow, Russian Federation;
Moscow Institute of Physics and Technology (State University),
Institutskii per. 9, 141700 Dolgoprudnyi, Moscow region,
Russian Federation;
Chernyshevskii Saratov State University,
ul. Astrakhanskaya 83, 410012 Saratov, Russian Federation
E-mail: nikitov@cplire.ru

D V Kalyabin, S A Osokin Kotel'nikov Institute of Radio Engineering and Electronics, Russian Academy of Sciences,
ul. Mokhovaya 11-7, 125009 Moscow, Russian Federation;
Moscow Institute of Physics and Technology (State University),
Institutskii per. 9, 141700 Dolgoprudnyi, Moscow region,
Russian Federation
E-mail: dmitry.kalyabin@phystech.edu, osokinserg@gmail.com

I V Lisenkov Kotel'nikov Institute of Radio Engineering and Electronics, Russian Academy of Sciences,
ul. Mokhovaya 11-7, 125009 Moscow, Russian Federation;
Moscow Institute of Physics and Technology (State University),
Institutskii per. 9, 141700 Dolgoprudnyi, Moscow region,
Russian Federation;
Oakland University, 2200 N. Squirrel Rd., Rochester, MI 48309, USA
E-mail: ivan.lisenkov@phystech.edu

A N Slavin Oakland University, 2200 N. Squirrel Rd., Rochester, MI 48309, USA

Yu N Barabanenkov Kotel'nikov Institute of Radio Engineering and Electronics, Russian Academy of Sciences,
ul. Mokhovaya 11-7, 125009 Moscow, Russian Federation
E-mail: barab624@mail.ru

A V Sadovnikov Kotel'nikov Institute of Radio Engineering and Electronics, Russian Academy of Sciences,
ul. Mokhovaya 11-7, 125009 Moscow, Russian Federation;
Chernyshevskii Saratov State University,
ul. Astrakhanskaya 83, 410012 Saratov, Russian Federation
E-mail: sadovnikovav@gmail.com

E N Beginin, M A Morozova, Yu P Sharaevsky
Chernyshevskii Saratov State University,
ul. Astrakhanskaya 83, 410012 Saratov, Russian Federation
E-mail: egbegin@gmail.com, mamorozovama@yandex.ru, SharaevskyYP@info.sgu.ru

Yu A Filimonov, Yu V Khivintsev, S L Vysotsky
Chernyshevskii Saratov State University,
ul. Astrakhanskaya 83, 410012 Saratov, Russian Federation;
Saratov Branch of Kotel'nikov Institute of Radio Engineering and Electronics, Russian Academy of Sciences,
ul. Zelenaya 38, 410019 Saratov, Russian Federation
E-mail: yuri.a.filimonov@gmail.com, khivintsev@gmail.com, vysotsl@gmail.com

V K Sakharov, E S Pavlov Saratov Branch, Kotel'nikov Institute of Radio Engineering and Electronics, Russian Academy of Sciences,
ul. Zelenaya 38, 410019 Saratov, Russian Federation
E-mail: valentin@sakharov.info, gekapavlov@gmail.com

Received 27 May 2015
Uspekhi Fizicheskikh Nauk **185** (10) 1099 – 1128 (2015)
DOI: 10.3367/UFNr.0185.201510m.1099
Translated by M N Sapozhnikov; edited by A M Semikhatov

1. Introduction

Recent extensive studies in the field of magnetic materials, in particular, magnetic micro- and nanostructures, have yielded interesting and important scientific results that form the basis for a new scientific direction called spintronics. Spintronics is a vigorously developing area of electronics that uses, notably, the transfer of magnetic moment or spin by an electric current in structures containing magnetic materials. The spin transfer can also occur with the help of magnons or spin waves in magnetic metals and dielectrics. This gives rise to a new scientific field, so-called magnonics — a field of spintronics or, more generally, electronics studying the physical properties of magnetic micro- and nanostructures, the properties of propagating spin waves, and the possibility of using spin waves to construct an elemental base for devices for data processing, communications, and storage based on new physical principles [1–9].

2. Experimental and theoretical methods for studying wave processes

2.1 Mandelshtam–Brillouin spectroscopy for studying magnetic structures

The space–time dynamics of spin-wave excitations in magnetically ordered media are often studied by optical probe methods, in particular, by the method based on Mandelshtam–Brillouin scattering (MBS) of light [10, 11]. The theoretical foundations of MBS in magnetically ordered media are considered in many papers (see, e.g., [12–15]) based on the wave or corpuscular approaches.

The wave approach is based on the magneto-optical scattering of a light wave in a magnetically ordered medium. Spin waves with the frequency f and wavelength λ propagating in a medium produce dynamic and spatial variations (small deviations from the equilibrium direction) in the magnetization $\mathbf{m}(f,\mathbf{r})$ of the medium (where $\mathbf{r}$ is the vector of spatial coordinates), resulting in variations in the permittivity ε. Spin waves in the medium produce a moving phase grating for a light wave, and light scattering is explained by the Bragg reflection of light from the diffraction grating and the Doppler shift of the reflected light frequency.

According to Bragg's law, the grating period Λ (equal to the spin wave length λ) is related to the Bragg angle φ_B and the incident light wavelength as

$$\sin\varphi_B = \frac{\lambda_0}{n\Lambda}\,, \tag{1}$$

where λ_0 is the light wavelength in the vacuum and n is the refractive index of light in the medium.

The Doppler effect is related to light scattering by a moving diffraction grating, the scattered light frequency being shifted from the incident light frequency f_0 by $\Delta f = f_0 \pm f$. The intensity of light scattered on a spin wave with a frequency f is [15]

$$I(f,\mathbf{r}) \sim \left|\mathbf{m}(f,\mathbf{r})\right|^2. \tag{2}$$

We can see from (2) that the scattered light intensity also depends on the deviation of the magnetization from equilibrium, i.e., on the spin-wave amplitude,

$$I(f,\mathbf{r}) \sim \varphi_0^2(f,\mathbf{r})\,. \tag{3}$$

In the corpuscular approach, MBS is considered as the scattering of photons by magnons (scattering of quasiparticles), to which the energy and momentum conservation laws can be applied. In this case, the main relations are

$$\begin{aligned} f_s &= f_0 + f\,,\\ \mathbf{k}_s &= \mathbf{k}_0 + \mathbf{k}\,, \end{aligned} \tag{4}$$

where f_s is the scattered light frequency, and $\mathbf{k}_s$, $\mathbf{k}_0$, and $\mathbf{k}$ are the respective wave vectors of the scattered and incident light and of the spin wave. The intensity of photons scattered by magnons with a frequency f is given by [16]

$$I(f) \sim D(f)\,n(f)\,, \tag{5}$$

where $D(f)$ and $n(f)$ are respectively the density of states and the Bose–Einstein distribution function for magnons at a given temperature.

The scattered light spectrum contains two components in general: the Stokes component at the frequency $f_0 - f$ and the anti-Stokes component at the frequency $f_0 + f$. The intensities of these components, which are determined by physical processes in magnetically ordered media, are different [17].

The choice of a particular approach (corpuscular or wave) is determined by experimental conditions. In particular, the wave approach is convenient if only the relative intensities I of scattered light are of interest.

Scheme and parameters of the experimental setup. Researchers at the Metamaterials Laboratory at Chernyshevskii Saratov State University have developed and started a facility for Brillouin spectroscopy of magnetic materials.

The applications of the facility in materials technology include the measurement of magnetic and acoustic properties of micrometer and submicrometer inorganic and semiconducting bulk and film samples, ferrite and permalloy films, multilayer structures and composite media [18–22], the physics of linear and nonlinear oscillations and waves [23–25], magnonics [2, 26–29], and spintronics [4, 5, 30–33].

The facility is mainly used for studying the space–time characteristics of spin-wave excitations in thin magnetic films and magnetic structures in the microwave range. The main parameters of the facility are: the range of measuring the frequency characteristics of scattered optical radiation is 1–100 GHz, the frequency range of measuring the characteristics of magnetic materials is 1–20 GHz, the time resolution is 1 ns, the spatial resolution is 250 nm–10 μm, and the range of magnetic fields produced is 100–10,000 Oe. A diagram of the facility is shown in Fig. 1.

The facility is based on a multipass tandem Fabry–Perot (TFP) interferometer [34] with a single-photon laser radiation detector (photon counter). The radiation source is a single-frequency laser emitting linearly polarized radiation at a wavelength of 532 nm. The laser beam is directed at a beamsplitter. Part of the beam is used as a reference beam to stabilize the interferometer, while another (signal) part is focused with a system of mirrors and lenses on the surface of the magnetic sample under study.

Samples are placed into a micropositioning system in a constant magnetic field directed tangentially to the sample plane. This system provides a scan of the sample surface by a focused laser beam.

A system of microstrip antennas (MSAs) is formed on the sample surface for exciting and receiving spin waves. A

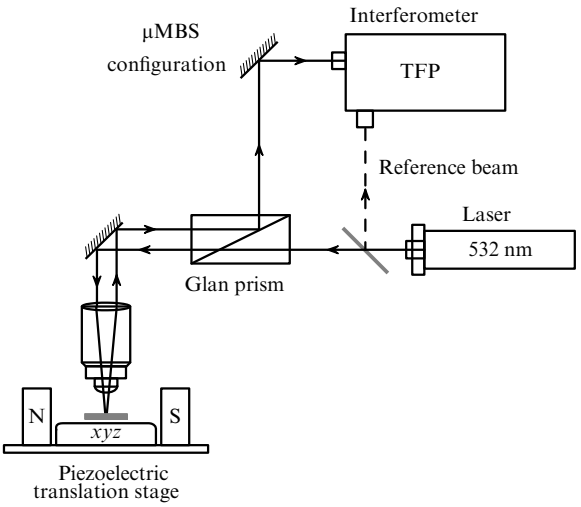

Figure 1. Schematic of the Mandelstam–Brillouin scattering setup. TFP: Tandem Fabry–Perot interferometer; μMBS (micro Brillouin light scattering): Brillouin light scattering with a 250 nm spatial resolution.

monochromatic or pulse-modulated microwave signal with a specified frequency f and power is fed to the antennas. Depending on the microwave signal frequency, strength, and orientation of the magnetic field, different-type (surface or bulk) spin waves with different dispersions (direct or inverse) can be excited in the magnetic structure [35–37]. Photons from the signal beam scattered by spin waves at different angles with different frequencies are directed to the interferometer for spectral analysis.

We must add that the intensity of scattered photons is determined by the instant amplitudes of spin-wave excitations; the spatial resolution of the method is determined by the minimal diameter of the focal spot of laser radiation on the surface of a magnetic sample and the penetration depth of laser radiation into the sample; hence, scattered photons contain information on the spatial characteristics of spin-wave excitations averaged over the sample thickness and the focal spot area.

2.2 Theoretical methods

2.2.1 Semianalytic methods.

Coupled wave method in the study of nonlinear phenomena in a magnon crystal. Nonlinear phenomena in periodic structures in microwave electronics and optics are often studied using the coupled mode method [37, 38]. A magnon crystal (MC) is a periodic structure with the wave number $k = 2\pi/L$, where L is the structure period, and the solution of the wave equation for a spin wave can be represented as an infinite sum of spatial harmonics [39].

The idea of the coupled wave method is that only the zeroth harmonics ($i = 0$) of forward waves and the -1st harmonics ($i = -1$) of backward waves may be taken into account in the first Brillouin zone ($0 \leqslant k_i L \leqslant 2\pi$), and the interaction of only these waves should be considered in the first Bragg resonance band [40]. The solution of the wave equation for the structure under study can be written as the sum of forward and backward waves:

$$m = A \exp\left[\mathrm{i}(\omega t - k_0 y)\right] + B \exp\left[\mathrm{i}(\omega t + k_{-1} y)\right], \qquad (6)$$

where A is the forward wave amplitude in the MC, B is the backward wave amplitude, and $k_{-1} = k_0 - 2\pi/L$.

Substituting (6) in the wave equation for the high-frequency components of the magnetization for a periodic structure and separating resonance terms, we obtain a system of equations for the amplitudes of the envelopes of forward and backward waves,

$$\begin{aligned} &\mathrm{i}\left(\frac{\partial A}{\partial t} + V\frac{\partial A}{\partial y}\right) + \eta_0 A + \chi_0 B + \gamma\left(|A|^2 + 2|B|^2\right)A = 0\,, \\ &\mathrm{i}\left(\frac{\partial B}{\partial t} - V\frac{\partial B}{\partial y}\right) + \eta_{-1} B + \chi_{-1} A + \gamma\left(|B|^2 + 2|A|^2\right)B = 0\,, \end{aligned} \qquad (7)$$

where γ is the nonlinearity coefficient, V is the group velocity, χ_0 is the coupling coefficient between the forward and backward waves, χ_{-1} is the coupling coefficient between the backward and forward waves, η_0 is the detuning from the frequency of the $i = 0$ mode in a single homogeneous film, and η_{-1} is the detuning from the frequency of the $i = -1$ mode in a single homogeneous film. Equations (7) are a system of nonlinear Schrödinger equations describing the linear and nonlinear couplings between waves in an MC. The values of these coefficients depend on the type of the magnetostatic wave (MSW) and the MC periodicity.

As an example, we consider an MC representing a ferromagnetic film with a saturation magnetization M_0, containing inhomogeneities produced on its surface in the form of grooves [41]. The thickness of the initial film is d_1, the groove depth is $\Delta d = d_1 - d_2$, the groove width is $a_2 = L - a_1$, and the structure period is L. We assume that the structure is infinite in the direction of the x and y axes. The constant magnetic field $\mathbf{H}_0$ is applied perpendicular to the structure surface and the forward volume MSW propagates along the y axis.

The film thickness in the periodic structure under study can be represented as $d = d_2 + \delta(y)$, where

$$\delta(y) = \delta(y + L) = \begin{cases} \Delta d = d_1 - d_2\,, & 0 \leqslant y \leqslant a_1\,, \\ 0\,, & a_1 \leqslant y \leqslant L\,. \end{cases}$$

Expanding $\delta(y)$ in a Fourier series and restricting the expansion to terms with $n = 0, \pm 1$, we can represent the last relation in the form [41]

$$d = d_0\left[1 + \delta d \cos\left(\frac{2\pi}{L}\, y\right)\right], \qquad (8)$$

where $d_0 = d_2 + \Delta d a_1/L$ and $\delta d = 2\Delta d/(\pi d_0)\sin(\pi a_1/L)$. Then the coefficients in (7) take the form [41]

$$\begin{aligned} &\gamma = \frac{\omega_H \omega_M}{2\omega}\left(1 + \frac{\omega_H^2}{\omega^2}\right), \qquad V = \frac{\omega_H \omega_M d_0}{4\omega}\,, \\ &\chi_{-1} = \delta d V \frac{k_{-1}^2}{k_0}\,, \qquad \chi_0 = \delta d V \frac{k_0^2}{k_{-1}}\,, \\ &\eta_0 = \frac{1}{2\omega}\left(\omega^2 - \omega_H^2 - \omega_H \omega_M \frac{k_0 d_0}{2}\right), \\ &\eta_{-1} = \frac{1}{2\omega}\left(\omega^2 - \omega_H^2 - \omega_H \omega_M \frac{k_{-1} d_0}{2}\right), \end{aligned}$$

where $\omega_H = \hat{\gamma} H_0$, $\omega_M = 4\pi\hat{\gamma} M_0$, H_0 is the external magnetic field strength, M_0 is the saturation magnetization, and $\hat{\gamma}$ is the gyromagnetic ratio [37]. In the particular case $k_0 = k_\mathrm{B}$, where k_B is the Bragg wave vector, $\eta_0 = \eta_{-1} = \eta$ and η_{-1} is the

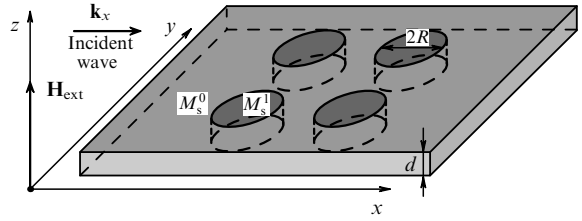

Figure 2. Ferromagnetic array with a system of inclusions.

detuning from the center of the forbidden zone of a single MC, and $\chi_0 = \chi_{-1} = \chi$ is the coupling coefficient between oppositely directed waveguides.

We can see from the equations and the values of the coefficients that the wave evolution in an MC is determined by the parameter δd characterizing the coupling between forward and reflected waves. For $\delta d = 0$, we obtain the equation for an MSW in a homogeneous film from (7) [37].

Multiple scattering method. We illustrate the multiple scattering method by considering the propagation of a forward volume MSW [36] in a metallized ferromagnetic plate containing an array of a finite number of ferromagnetic cylindrical inclusions [42], although this method can also be generalized to the case of an unbounded MC [43]. We consider a ferromagnetic matrix of thickness d with the saturation magnetization M_s^0 (Fig. 2). Cylindrical inclusions with radius R consist of a ferromagnetic material with the saturation magnetization M_s^1. An external magnetic field H_{ext} is applied along the z axis normally to the matrix. By neglecting the crystalline surface anisotropy, the effective field inside the sample can be written as $H = H_{\text{ext}} - H_{\text{dm}}$, where the demagnetizing field H_{dm} is defined as $4\pi M_s^0$ and $4\pi M_s^1$ [43] for the ferromagnet in the matrix and inclusion, respectively. The problem is solved by using the Walker equation [36] obtained from Maxwell's equations in the magnetostatic approximation and having the form

$$\mu_0^t(\partial_x^2 + \partial_y^2)\Psi^t + \partial_z^2\Psi^t = 0\,. \tag{9}$$

Here, $\Psi^t(x,y,z)$ is the magnetostatic potential related to the magnetic field vector $\mathbf{h}$ as $\mathbf{h} = -\nabla\Psi^t$. We let $\mathbf{b} = \overleftrightarrow{\mu}\,\mathbf{h}$ denote the magnetic induction vector, where the antisymmetric magnetic permeability tensor $\overleftrightarrow{\mu}$ of the ferromagnet is specified by the diagonal, μ_0, and nondiagonal, $\mathrm{i}\mu_a$, components. The index $t = 0$ in Eqn (9) and below is related to variables in the ferromagnetic matrix (Ψ^0, μ_0^0, μ_a^0, and $\mathbf{b}^0$ describe the wave process outside inclusions), the index $t = 1$ is related to variables inside inclusions, and the index t is used for a description in the general form. Using the boundary conditions $b_z^t = 0$ on metallized surfaces $z = 0$ and $z = d$ and separating the variables in the magnetostatic potential $\Psi^t(x,y,z) = \Psi^t(x,y)\cos(k_z z)$, where $k_z = n\pi/d$, $n = 0, 1, 2, \ldots$, we obtain

$$(\partial_x^2 + \partial_y^2)\Psi^t + (k_r^t)^2\Psi^t = 0\,. \tag{10}$$

This equation involves the planar component $k_r^t = \sqrt{-1/\mu_0^t}\,k_z$ of the wave vector. The solution of Eqn (10) with boundary conditions on the inner surfaces of inclusions gives the magnetostatic potential $\Psi^t(x,y,z)$ inside the ferromagnetic matrix and ferromagnetic inclusion.

We consider the scattering of a plane spin wave $\Psi^{\text{inc}}(r) = \exp(\mathrm{i}\mathbf{k}_r^0\mathbf{r})$ by a system of N cylindrical inclusions.

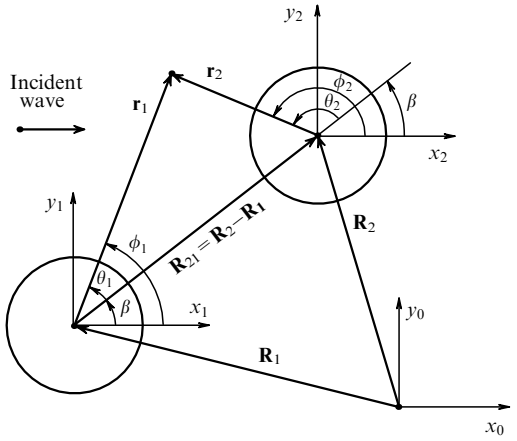

Figure 3. Constructing local coordinate systems for two cylindrical inclusions.

Each jth inclusion is related to its local coordinate system with the center $\mathbf{R}_j$ coinciding with the cylinder center and calculated with respect to the laboratory coordinate system (Fig. 3). All local coordinate systems are obtained by a parallel displacement of the laboratory system along its axes x_0 and y_0 with the unit vectors $\hat{\mathbf{x}}$ and $\hat{\mathbf{y}}$, and $\mathbf{k}_r^0 = k_r^0\hat{\mathbf{x}}$. The propagating plane spin wave can be expanded in scalar cylindrical wave functions as

$$\Psi^{\text{inc}}(r_j, \phi_j) = \sum_{m=-\infty}^{\infty} A_{jm} J_m(k_r^0 r_j)\exp(\mathrm{i}m\phi_j)\,. \tag{11}$$

Here, r_j and ϕ_j are the local cylindrical coordinates of the observation point, and $J_m(u)$ is the Bessel function with the cylindrical multipole index m. The coefficient $A_{jm} = \varepsilon_j \mathrm{i}^m$ contains the phase factor $\varepsilon_j = \exp(\mathrm{i}\mathbf{k}_r^0\mathbf{R}_j)$ depending on the position of the center of the jth cylinder in the laboratory coordinate system. The scattering of the propagating wave results in the appearance of the scattered, Ψ^{scat}, and refracted, Ψ^{trans}, fields around and inside each inclusion:

$$\Psi_j^{\text{scat}}(r_j, \phi_j) = \sum_{m=-\infty}^{\infty} B_{jm} H_m(k_r^0 r_j)\exp(\mathrm{i}m\phi_j)\,, \tag{12}$$

$$\Psi_j^{\text{trans}}(r_j, \phi_j) = \sum_{m=-\infty}^{\infty} X_{jm} J_m(k_r^0 r_j)\exp(\mathrm{i}m\phi_j)\,, \tag{13}$$

where B_{jm} and X_{jm} are the respective scattering and refraction coefficients and $H_m(u)$ is the Hankel function. To define the boundary conditions on the inner surfaces of inclusions corresponding to the continuity of the normal component of the magnetic induction vector and the tangential component of the magnetic field vector, the total field near the surface of each inclusion must be known. For example, the total field around the first inclusion for a system of two inclusions has the form

$$\Psi_1^{\text{scat+inc}}(r_1, \phi_1) = \Psi_1^{\text{scat}}(r_1, \phi_1) + \Psi_1^{\text{inc}}(r_1, \phi_1) + \Psi_{21}^{\text{scat}}(r_2, \phi_2)\,. \tag{14}$$

A specific feature of the potential component Ψ_{21}^{scat} of a spin wave incident on the first inclusion and scattered by the second inclusion is a representation in the coordinate system of the second inclusion. To pass to the coordinate system of

the first inclusion, the summation theorem for cylindrical functions is used [44]:

$$\exp(\mathrm{i}n\theta_2)H_n(k_r^0 r_2) = (-1)^n \sum_{l=-\infty}^{\infty} H_{n+l}(k_r^0 R_{12})\, J_l(k_r^0 r_1)\exp(-\mathrm{i}l\theta_1)\,, \quad (15)$$

where θ_1 and θ_2 are shown in Fig. 3, $\mathbf{R}_{jj'} = \mathbf{R}_j - \mathbf{R}_{j'}$ is the vector distance between the centers of the jth and j'th inclusions, and $R_{jj'} = |\mathbf{R}_{jj'}|$. By applying summation theorem (15) to equality (14), we can determine boundary conditions on the inner surface of each inclusion and obtain a closed system of equations for the self-consistent scattering coefficients B_{jm} of inclusions in the physically transparent form

$$B_{jm} = B_m^{(j)} + \frac{B_m^{(j)}}{A_{jm}} \sum_{j\neq j'=1}^{N} \sum_{l=-\infty}^{\infty} G_{m-l}^{jj'} B_{j'l}\,, \quad j = 1, 2, \ldots, N\,,$$
$$G_{m-l}^{jj'} = \exp\left[\mathrm{i}(l-m)\arg\mathbf{R}_{jj'}\right] H_{l-m}(k_r^0 R_{jj'})\,, \quad (16)$$

where $B_m^{(j)}$ is the scattering coefficient of the isolated jth inclusion and the ratio $T_m^{(j)} = B_m^{(j)}/A_{jm}$ determines the scattering matrix of the isolated jth inclusion. The phase factor $\arg\mathbf{R}_{jj'}$ in the matrix kernel $G_{m-l}^{jj'}$ specifying the angle between the vector $\mathbf{R}_{jj'}$ and the unit vector $\hat{\mathbf{x}}$ (see Fig. 3) is the phase increment of the spin wave on the path between the jth and j'th inclusions. The second factor in the matrix kernel is the component of the Green's function of two-dimensional Walker equation (10).

To solve the system of equations (16) by iterations, we represent it in the form

$$B_{jm} - T_m^{(j)} \sum_{j\neq j'=1}^{N} B_{j'm} H_0(k_r^0 R_{jj'}) = \tilde{B}_{jm}\,. \quad (17)$$

The left-hand side of Eqns (17) contains only the m-multipole terms. The right-hand side, which is easily reproduced, describes the effect of the propagating spin wave in the term $B_m^{(j)}$ and contributions from all other multipoles $m \pm \delta m$ appearing during the scattering of the spin wave.

In this paper, we are interested in the case of a periodic arrangement of the centers of N cylindrical inclusions along a circle with radius r. We first consider an auxiliary problem for the eigenmodes $U^{(j)}$ and eigenvalues $\lambda_j^{(m)}$ in the single-multipole approximation by writing

$$U^{(j)} - \sum_{j\neq j'=1}^{N} a_{jj'}^{(m)} U^{(j')} = \lambda_j^{(m)} U^{(j)}\,,$$
$$a_{jj'}^{(m)} = T_m^{(j)} H_0(k_r^0 R_{jj'})\,, \quad (18)$$

where $a_{jj'}^{(m)}$ is the coupling matrix of the inclusions. The eigenvectors $U^{(j)}$ of system (18) can be written in the form of N-component vectors

$$U^{(j)} = (1, p_j, p_j^2, \ldots, p_j^{N-1})\,,$$
$$p_j = \exp\left(\mathrm{i}\,\frac{2\pi j}{N}\right), \quad j = 1, 2, \ldots, N\,. \quad (19)$$

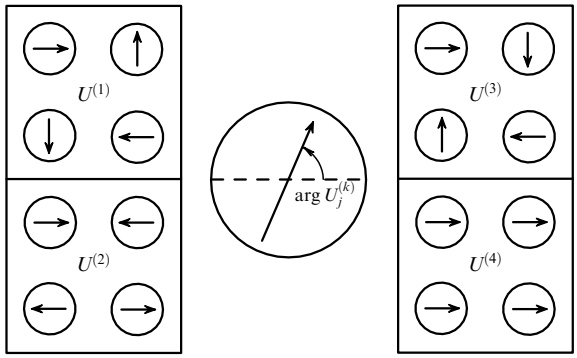

Figure 4. Illustration of phase shifts formed by the kth eigenvector $U_j^{(k)}$ of the magnetostatic potential of a spin wave scattered by the jth cylinder. Each arrow indicates $\arg U_j^{(k)}$.

The components $U_k^{(j)}$, $k = 1, 2, \ldots, N$ of each jth eigenvector are equal to unity in modulus, $|U_k^{(j)}| = 1$, and differ in the values of arguments $\arg U_k^{(j)}$ (Fig. 4). The eigenvalues $\lambda_j^{(m)}$ corresponding to eigenvectors (19) are expressed in the case of an even number of inclusions $N = 2n$ by the sums

$$\lambda_j^{(m)} = 1 - \sum_{j'=1}^{n} v_{jj'} a_{11+j'}^{(m)}\,,$$
$$v_{jj'} = 2\cos\frac{\pi jj'}{n}\,,$$
$$j' = 1, \ldots, n-1\,, \quad v_{jn} = (-1)^j\,. \quad (20)$$

Eigenvectors (19) are pairwise orthogonal, $\langle U^{(j)}|U^{(j')}\rangle = N\delta_{jj'}$, which allows us to represent the system of equations (17) in the compact form

$$B_{jm} = \frac{1}{N}\sum_{k=1}^{N} \langle\tilde{B}|U^{(k)}\rangle\, \frac{U_j^{(k)}}{\lambda_k^{(m)}}\,, \quad (21)$$

where the summation in the right-hand side is performed over the eigenvectors, labeled by k, and the subscript j labels the eigenvector component.

System of equations (21) suggests a direct approach to solving the problem of the excitation of eigenmodes (19) by a propagating spin wave. For example, if the spin wave length is large compared to the radius of a circular cluster of $N = 4$ inclusions, the propagating wave mainly excites the 'isotropic' $U^{(4)} = (1, 1, 1, 1)$ mode (see Fig. 4) with the same phase shifts of the potential during the spin wave scattering by all four inclusions.

System of equations (21) is especially convenient for using the iteration method. The first step of the iteration solution is the substitution $\tilde{B}_{jm} = B_{jm}^{(j)} = \mathrm{i}^m T_m \varepsilon_j$, which is obvious, taking system of equations (16) into account. For the problem with $N = 4$ cylindrical inclusions, the first iteration approximation gives the following expression for the magnetostatic potential (12) of the spin wave scattered by the jth inclusion:

$$\Psi_j^{\mathrm{scat}}(r_j, \phi_j) = \sum_{k=1}^{4} \Psi_{kj}^{\mathrm{scat}}(r_j, \phi_j)\,,$$
$$\Psi_{kj}^{\mathrm{scat}}(r_j, \phi_j) = \frac{1}{4}\,\varepsilon^{(k)} U_j^{(k)} \sum_{m=-\infty}^{\infty} \mathrm{i}^m\, \frac{T_m}{\lambda_k^{(m)}}\, H_m(k_r^0 r_j)\exp(\mathrm{i}m\phi_j)\,. \quad (22)$$

The factors $\varepsilon^{(k)}$ are linear combinations of the phase factors $\varepsilon_j = \exp(\mathrm{i}\mathbf{k}_r^0\mathbf{R}_j)$ depending on the position of the jth inclusion in the laboratory coordinate system:

$$\begin{aligned}
\varepsilon^{(1)} &= \varepsilon_1 - \varepsilon_3 - \mathrm{i}(\varepsilon_2 - \varepsilon_4)\,,\\
\varepsilon^{(2)} &= \varepsilon_1 - \varepsilon_2 + \varepsilon_3 - \varepsilon_4\,,\\
\varepsilon^{(3)} &= \varepsilon_1 - \varepsilon_3 + \mathrm{i}(\varepsilon_2 - \varepsilon_4)\,,\\
\varepsilon^{(4)} &= \varepsilon_1 + \varepsilon_2 + \varepsilon_3 + \varepsilon_4\,.
\end{aligned} \tag{23}$$

2.2.2 Numerical simulation. Numerical simulation of the propagation of MSWs in periodic, quasiperiodic, and irregular magnetic microwaveguides is very important because the analytic solution of the equations for the MSW dynamics in such structures cannot be obtained without significant simplifications.

A numerical analysis of MSW propagation in periodic ferrite waveguide structures with a finite width can be performed by considering processes at a fixed frequency using methods applicable in a given frequency region, for example, the finite-element method (FEM) [45–51] or methods operating in the time representation, for example, the finite difference time domain (FDTD) method [52–55].

The FEM involves a decomposition of the calculation region into finite elements (in the simplest case, triangles). The field components within each finite element are approximated by simple polynomials. The coefficients of polynomials are expressed in terms of the field component values at a finite number of points lying on the boundary and inside the element. The discretization of partial differential equations is performed by one of the methods appropriate for each particular problem. We used the variation approach. After discretization, the problem reduces to solving a generalized eigenvalue problem for large sparse matrices. Solving the eigenvalue problem yields the field distribution of the eigenmode and its frequency, i.e., a point on the dispersion characteristic. By repeating calculations for the required number of points in the specified frequency range, we can calculate the total dispersion characteristic and the corresponding field distributions. Such an approach is efficient for calculating the eigenfrequencies and fields of resonator eigenmodes, dispersion characteristics, and the eigenwave fields propagating in magnetic structures.

The propagation of spin waves in ferromagnetic waveguide irregular microstructures can be numerically simulated by solving the Landau–Lifshitz equation by the FDTD method. This numerical micromagnetic simulation method, which has been successfully used for solving problems of the excitation and propagation of spin waves in regular and irregular magnetic metal and dielectric microstructures [6, 56, 57], is more efficient for studying scattering problems and the propagation of wave packets in dispersive media and nonlinear structures. The freely available mumax3 software code [54, 55] allows calculations on modern multicore processors and cluster computer systems containing graphic processors and supporting the CUDA (Computer Unified Device Architecture) technology, which significantly reduces the FDTD calculation time of the nonstationary propagation dynamics of spin waves in ferromagnetic micro- and nanostructures.

3. Application of magnetic structures in signal processing and communication systems

3.1 Distributed periodic systems

3.1.1 One-dimensional magnonic crystals.

Nonlinear phenomena in MCs. One of the main aspects in the study of nonlinear processes in MCs is the analysis of soliton formation mechanisms [58, 59], which is relevant not only from the standpoint of fundamental science but also for applications, namely, for data processing and transfer in telecommunication systems.

Experimental results and the results of numerical simulations based on a single nonlinear Schrödinger equation (NSE) are presented in [58, 59]. The dispersion and nonlinearity coefficients in this equation were calculated assuming that in a ferromagnetic film, one magnetostatic wave propagates with the dispersion depending on the parameters of the periodic structure.

However, fiber optic gratings are often studied by the coupled-mode method (see Section 2.2.1) assuming that nonlinear wave processes in such periodic structures near the forbidden zone are mainly caused by a superposition of the incident and reflected waves and using a system of coupled NSEs for their description.

Stationary solutions in the form of envelope solitons obtained from a system of coupled NSEs were called Bragg solitons [40]. Of special interest are the studies of solitons of a new type (slit solitons), which can propagate in the forbidden band with a group velocity much lower than the soliton propagation velocity in a homogeneous nonlinear medium [40, 60].

In the weak nonlinearity approximation (see Section 2.2.1), a system of NSEs for the envelopes of forward and backward waves can be written in form (7) [41, 61]. Equations (7) are analogous to the system of two coupled NSEs describing the propagation of incident and reflected waves in Bragg optical gratings [40, 60] and represent a system with an incoherent coupling.

The numerical solution of the obtained system showed the possibility of forming Bragg-like solitons in MCs with different properties, in particular, solitons with a zero velocity and solitons localized on a limited length of the structure. The main formation mechanism of such solitons is the mutual trapping of pulses in forward and backward waves, which propagate with the same velocity (which, in turn, is determined by the relative power of the two waves), and the power transfer between forward and backward waves determined by the coupling coefficient between them.

Figure 5a demonstrates the formation of a Bragg-like soliton in an MC, calculated by numerically solving the system of coupled NSEs (6) by the split-step Fourier method (SSFM) in the case of excitation of magnetostatic surface waves (MSSWs) for the detuning $\eta = 1$. As the initial conditions, the pulse was specified only on the forward wave in the form $\varphi_\mathrm{f}(y,0) = \varphi_0 \exp(-y^2/y_\mathrm{pulse}^2)$, $\varphi_\mathrm{b}(y,0) = 0$, where y_pulse is the pulse width and φ_0 is the dimensionless pulse amplitude at the initial instant. For the chosen value of the coupling coefficient χ, a complete power transfer occurs between forward and backward waves with a period T (Fig. 5a). In this case, first, a pulse propagating in the positive direction along the y axis is formed on the forward wave (see Fig. 5c and grey curves in Fig. 5b). The power immediately

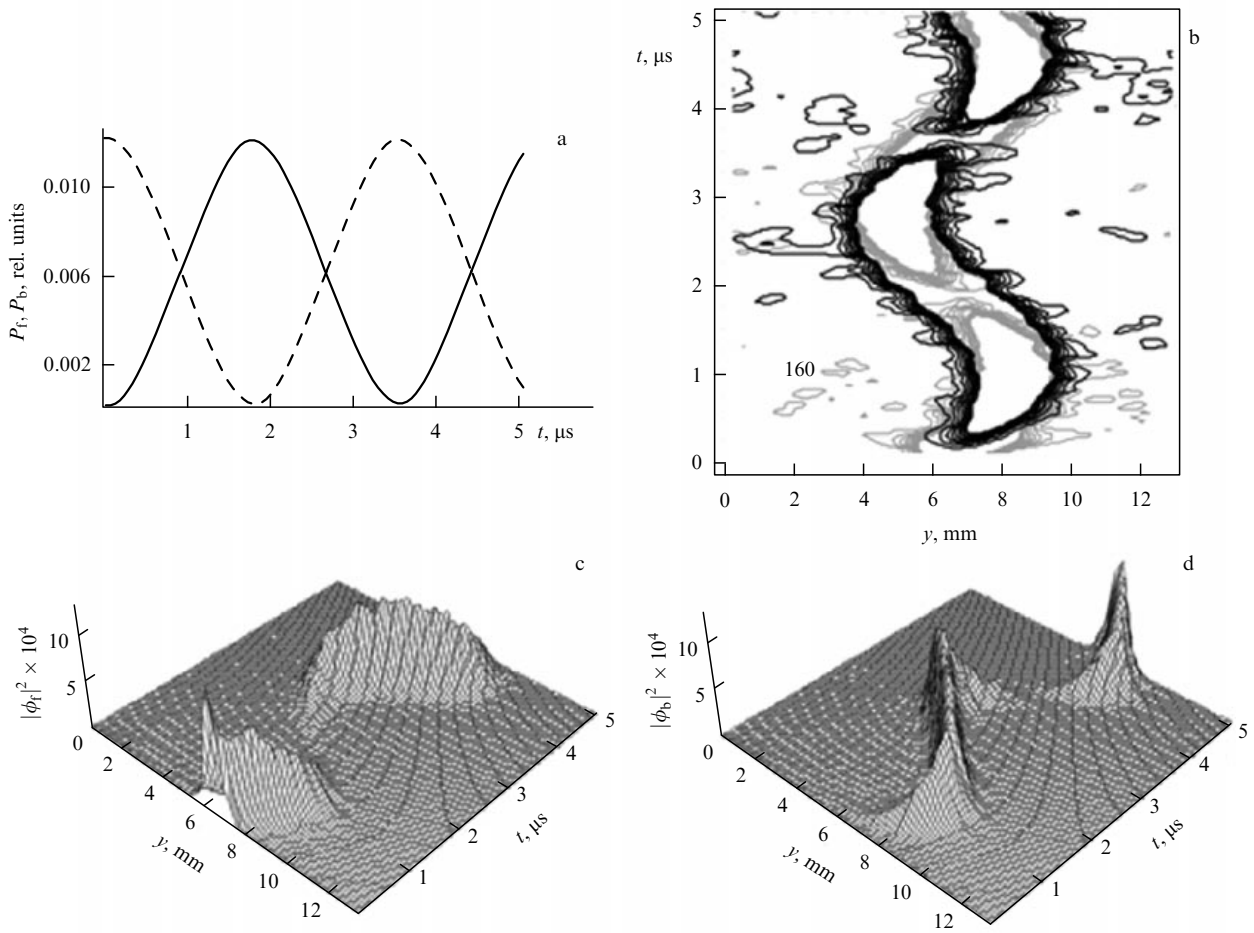

Figure 5. (a) Changes in the forward-wave power P_f (dashed curve) and backward-wave power P_b (solid curve) with time. (b) Level lines for the amplitudes of envelopes φ_f (grey lines) and φ_b (black lines). (c) Space–time evolution of envelopes (c) φ_f and (d) φ_b for $\chi = 2.5 \times 10^6$ s^{-1}, $V = 0.3 \times 10^6$ cm s^{-1} ($\varphi_{0f} = 0.04$, $\varphi_{0b} = 0$).

transfers to the backward wave pulse (see Fig. 5d and black curves in Fig. 5b) propagating in the same direction.

After the time interval $T/2$, the powers of pulses on forward and backward waves equalize, and the pulses stop. Thus, the pulses periodically change their direction with time, moving to the higher-power wave, remaining nevertheless localized on some length of the structure. In this case, the combination of pulses on forward and backward waves forms a common structure propagating with a common velocity like a Bragg soliton [40].

Below, we present the results of experimental studies of the formation of soliton-like pulses in the forbidden zone of a one-dimensional MC during the propagation of MSSWs at frequencies below 4 GHz for which three-magnon decay processes are possible [62, 63]. Pulse characteristics obtained in experiments are compared with the results of the numerical calculation of slit solitons in the coupled NSEs for a bounded MC.

The MC under study contains a periodic system of grooves with a rectangular profile obtained by photolithography on the surface of an yttrium iron garnet (YIG) film grown on a gadolinium–gallium garnet (GGG) substrate. The sample size was $4 \times 5 \times 0.5$ mm, the saturation magnetization of the film was $4\pi M_0 = 1750$ G, and the film thickness was $d_1 = 4$ μm. The parameters of the periodic structure were the groove depth, width, and period: $\Delta d = d_1 - d_2 = 0.7$ μm, $a_2 = 70$ μm, and $L = 100$ μm, respectively. The characteristics of MSSWs propagating in the MC were studied with a setup containing an Agilent DSO81004B real-time oscilloscope and an Anritsu MG3692C microwave generator.

Figure 6 presents the results of a study of the propagation of rectangular 260 ns microwave pulses propagating in a structure with the pulse repletion period $\tau_s = 4$ μs and the carrier frequency f_0 coinciding with the central frequency of the first forbidden zone of the MC. The time realizations of the microwave signal at the structure output for different input powers $P_{in} = -5 - 16$ dBmW are shown in Fig. 6a. The output signal is a train of pulses, their number and peak amplitude depending on P_{in}.

In the linear regime (for $P_{in} = -5$ dBmW), two weak pulses with identical amplitudes corresponding to the leading edge and the trailing edge of the input rectangular pulse are observed, the interval between pulses being equal to the input pulse duration. As the input signal power increases, an additional pulse appears between these two pulses. The amplitude and phase of the input signal envelope for three input powers are shown in Figs 6b–d. We can see that as the input power is increased, the phase inclination angle inside the additional pulse decreases and, for $P_{in} = 16$ dBmW (Fig. 6a), the phase inside the additional pulse has a characteristic 'ledge'. In this case, we can assume that the additional pulse has the properties of a slit soliton [40]. As the input signal power is increased further, the phase inside the pulse changes its slope and becomes decreasing (Fig. 6d).

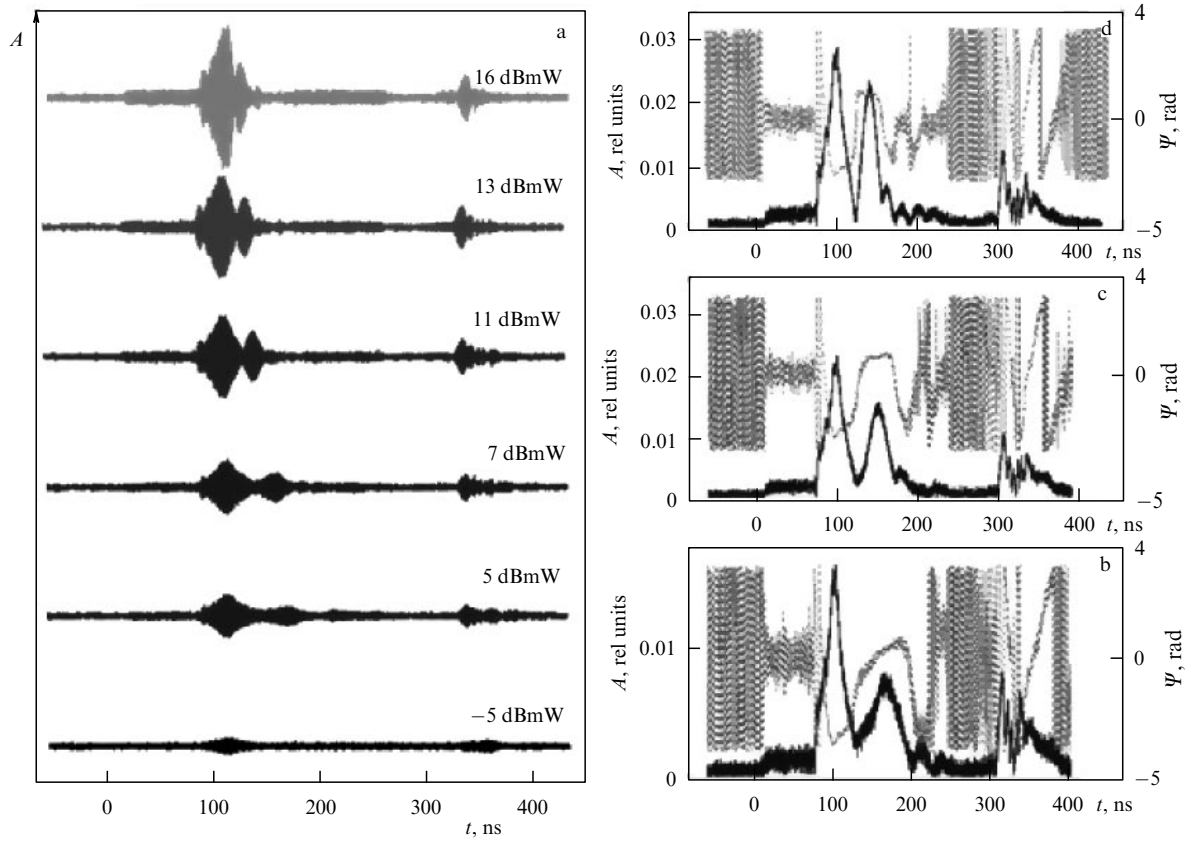

Figure 6. (a) Time realizations of the output signal for different input power levels. The envelope amplitude (dark curve) and phase (grey curve) of the transmitted signal for the input powers (b) $P_{in} = 14$, (c) 16, and (d) 18 dBmW.

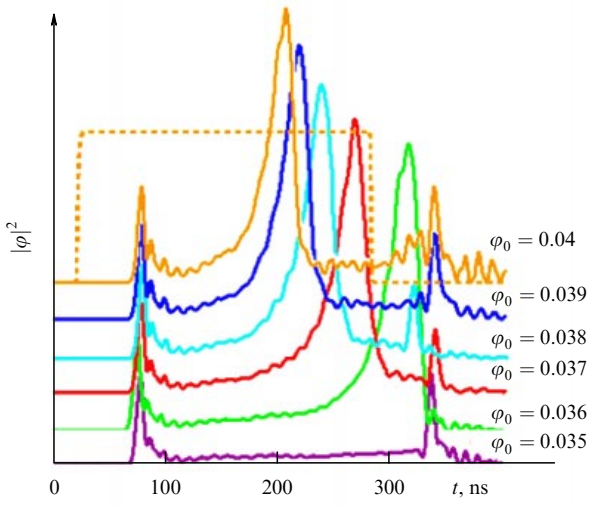

Figure 7. Time dependences of the input signal envelope for $y = l$ for different amplitudes φ_0 of a rectangular input signal (dotted curve for $y = 0$).

Figure 7 shows the results of the numerical solution of system of equations (7) for a bounded MC for different amplitudes of a rectangular input signal. We can see that the output-signal formation dynamics are analogous to the experimental dynamics: for a small amplitude of the input signal, the pulse is almost completely reflected from the MC, as from a linear Bragg grating, i.e., the output signal contains only two pulses separated by an interval equal to the input pulse duration. These pulses are the result of differentiating the leading edge and the trailing edge of the input rectangular pulse. As the input amplitude increases (for $\varphi_0 = 0.037$), an additional pulse appears between the two pulses in the output signal. With a further increase in the input amplitude, the additional pulse approaches the first pulse of the output signal, i.e., its velocity increases.

It has been shown that soliton-like pulses can be generated in the forbidden zone of a one-dimensional MC during the propagation of MSSWs at frequencies below 4 GHz at which three-magnon decay processes are possible. The generation of pulses is observed upon increasing the input power. The pulse velocity, which is smaller than the group velocity of surface waves in a homogeneous film, increases with increasing the amplitude. The generation of soliton-like pulses in MCs is well described in the coupled-wave theory by a system of coupled NSEs for the envelopes of direct and counter waves in a periodic structure.

3.1.2 Magnonic crystal with distributed defects. One of the methods for controlling forbidden zones in an MC is the introduction of defects, which are produced in the periodic structure either by violating its periodicity in some region of size comparable with the spatial period of the MC (local defects) or by creating a homogeneous region with dimensions greatly exceeding the MC period (distributed or line defects).

Many papers have been devoted to the study of the influence of local defects on characteristics of the forbidden zones in MCs (see, e.g., [64, 65] and the references therein). It was shown in these papers that local defects can be produced

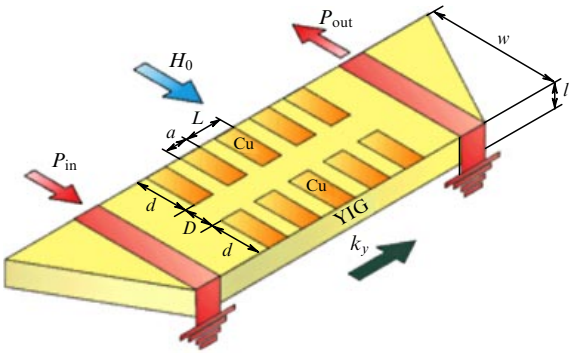

Figure 8. Schematic of an MC with distributed defects.

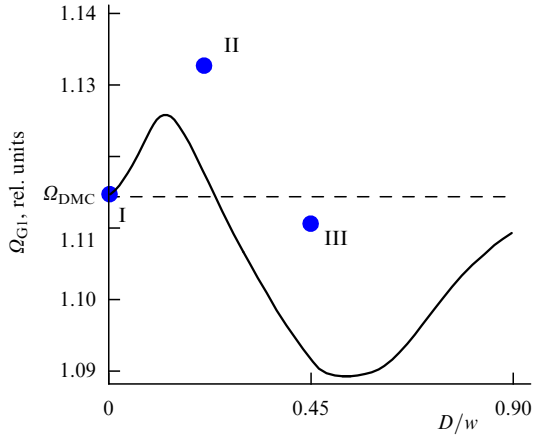

Figure 9. Dependence of the central frequency of the forbidden band on D/w.

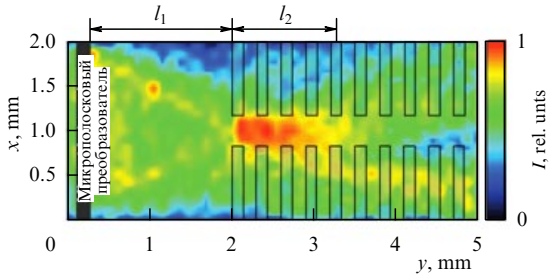

Figure 10. Two-dimensional distribution of the scattered light intensity I proportional to the magnetization amplitude squared, measured at the central frequency of the forbidden band of sample III (obtained by the method described in Section 2.1).

in a one-dimensional MC by introducing a layer with other parameters or defect grooves (pegs) [67] into a multilayer MC [64, 66] or removing one or several holes (pegs) in a two-dimensional MC [65]. The presence of such defects leads to the formation of narrow transmission bands in forbidden zones. Unlike MCs with local defects, the study of MCs with distributed defects started recently and to date only two papers [65, 66] have been published in this field. It is shown in these papers that the presence of a distributed defect in a periodic structure leads to the disappearance of the forbidden band in the spectrum of spin waves and the localization of the signal in the region of the distributed defect in the spin-wave propagation direction. Such a situation is observed in a two-dimensional micrometer MC based on a YIG film [68] and a two-dimensional nanometer MC based on a CoFe film [69]. However, of interest is the study of characteristics of forbidden zones in one-dimensional MCs with a distributed defect. In this case, a wave propagates over the entire width of the periodic structure in one direction. The forbidden zone should be preserved in this case. The phase velocity of the spin wave in the structure is determined not only by the structure period but also by the geometric parameters of the distributed defect, resulting in a frequency shift of the forbidden zone.

In this section, we demonstrate the possibility of controlling forbidden zones in a one-dimensional MC with a distributed defect by changing the geometric dimensions of the distributed defect. The one-dimensional MC is one with periodic boundary conditions based on a homogeneous YIG film containing a periodic system of metal strips on its surface (Fig. 8). The distributed defect is a region of the YIG film of width D with homogeneous boundary conditions, which is created along the propagation direction of spin waves and has dimensions greatly exceeding the MC period.

We studied three MC samples in our experiments. Sample I was an MC without a distributed defect ($D = 0$). Samples II and III were MCs with distributed defects with respective widths $D = 200$ μm and 1 mm.

Figure 9 demonstrates the influence of the width D of the distributed defect on the forbidden zone position. The circles show the experimental central frequencies of forbidden bands for the three samples. For $D = 0$ (point I in Fig. 9), the forbidden band is located at the frequency Ω_{DMC}. As D increases, the frequency Ω_{G1} first increases (point II) and exceeds Ω_{DMC} and then decreases, becoming lower than Ω_{DMC} (point III).

These experimental results show that (1) the forbidden band shift in the spectrum of excited spin waves depends in a complicated way on geometrical parameters of a distributed defect, in particular, on the width of the homogeneous region of the MC (see Fig. 9); and (2) the waveguide propagation of the spin wave occurs at some distance along the distributed defect (Fig. 10). It can be expected that if the length of the structure is limited by $l_1 + l_2$, the signal would propagate through the MC with a distributed defect and the forbidden band would not be observed in the amplitude–frequency characteristic of such a transmission line.

The model was constructed assuming that the system under study can be considered as a structure consisting of two identical magnonic crystals MC_1 and MC_2 of width d separated with a homogeneous film of width D. The coupled-wave method (see Section 2.2.1) applied in the linear case can be used to construct a model that agrees well with the experimental data.

Figure 9 shows the dependence (curve) of the central frequency of the forbidden band on the distributed defect width D for model parameters corresponding to experimental data.

3.1.3 Irregular waveguide with a periodically changing width. Spin waves propagating in one- and two-dimensional planar ferromagnetic structures with periodically spatially modulated parameters are being actively investigated presently [70]. Periodic structures can be created by different methods such as the spatial variation of magnetic properties of materials (for example, the saturation magnetization) [71], the change in the thickness or width of planar waveguide magnetic structures [72–74], the preparation of two-dimensional magnetic gratings [2], and the spatial modulation of static

magnetic fields [75]. Such periodic structures, called magnonic crystals [70, 72], are characterized by the presence of forbidden bands at frequencies for which the Bragg condition $k_B = n\pi/L$ is satisfied, where L is the structure period, k_B is the Bragg wave number, and n is the order number of a forbidden band. The parameters of forbidden bands (depth and frequency width) depend, in particular, on the relative modulation depth of spatial parameters $\xi = \Delta w/w_0$, where Δw is the parameter variation and w_0 is its average value.

Magnonic crystals can be used as an elemental base for manufacturing various functional devices for signal processing in the microwave range: resonators, couplers, delay lines, filters, phase shifters, etc. The best theoretically and experimentally studied are one-dimensional MCs (with medium parameters or dimensions varying only along one of the directions) based on waveguides with a constant width with characteristic transverse dimensions 2–3 mm and weak modulation $\xi < 0.1$. The propagation of waves in such MCs can be assumed to be single-mode, and the scattering of waves by inhomogeneities occurs without the excitation of higher modes.

The miniaturization of the elemental base and creation of integrated circuits for data processing systems require passing to the micrometer and submicrometer spatial MC scale with a simultaneous reduction in the wavelength of propagating waves. In this range of spatial scales, the main type of waveguide structures used in one-dimensional MCs is permalloy film waveguides.

Magnonic crystals based on waveguides with a periodically changing width were studied experimentally and theoretically in [76, 77]. The value of ξ for MCs of this type determines the relative modulation depth of the waveguide width. For small modulation depths $\xi < 0.1$, such structures can be analyzed in the single-wave approximation. But even in this case, the excitation and propagation of waves in transversely bounded MCs is substantially multimode, the spectrum of transverse wave numbers is quantized, and branches corresponding to the so-called width modes appear in the dispersion characteristics $\omega(k)$ of waves. As the waveguide width w is reduced for a fixed frequency ω, the mode spacing Δk in wave numbers between branches increases. In regular waveguides, these modes propagate independently. But in modulated-width waveguides, the increase in the modulation depth ξ can lead to the coupling of width modes scattered by inhomogeneous waveguide boundaries. For strong modulation ($\xi > 0.1$), the intermode interaction of propagating waves in the formation of forbidden bands should be taken into account [78].

Thin YIG films whose dissipation parameters are considerably smaller than those of permalloy are broadly used to create MCs and controllable devices in spintronics and magnonics [2, 27]. As the transverse size of regular YIG waveguides is decreased to a few hundred micrometers, the propagation of waves becomes multimode.

It is of interest to study the features of the formation of forbidden bands in MCs based on YIG waveguides with the periodically modulated width and spatial intensity distribution of spin-wave excitations at different frequencies. Magnonic crystals based on waveguides typically consist of connected regular and periodic waveguide structures having different eigenwave spectra, the waves being excited by microstrip antennas located in the regular waveguide.

We consider an irregular YIG waveguide consisting of two sections connected with a YIG waveguide with a linearly changing width. The first section is a broad waveguide in which spin waves are excited by a microstrip antenna. The second section is an MC based on a narrow waveguide with a periodically modulated width. The waveguide with the variable width serves as a conforming element [79] and can be used to control the mode composition of spin waves propagating in the MC region [28, 80].

The spatial distribution of wave amplitudes can be measured by different methods, for example, with the help of microwave probes. However, as the dimensions of the waveguides decrease (below 500 μm), the spatial resolution of probe methods becomes insufficient. At present, the spatial and temporal characteristics of waves in micrometer and submicrometer waveguides are often studied by the method of Mandelshtam–Brillouin scattering (MBS) from magnetic excitations in ferromagnetic structures [81]. Below, we present the results of MBS studies of the formation of forbidden bands and multimode propagation of MSWs in one-dimensional MCs in different frequency regions.

Magnonic crystals were fabricated using a 10 μm thick single-crystal YIG film with the saturation magnetization $4\pi M_0 = 1350$ G grown on a 500 μm thick GGG substrate. On the GGG film surface, an irregular waveguide for magnetostatic waves was fabricated by the laser scribing method [28], by connecting two regular waveguides of widths $w_0 = 2000$ and 353 μm via the waveguide region with linearly changing width (Fig. 11). Laser cutting was performed with an ytterbium-doped fiber laser emitting 1060 nm, 25 ns, and 0.05 mJ pulses at a pulse repetition rate of 20 kHz. In the narrow waveguide, a one-dimensional MC was similarly fabricated with a periodic sequence of rectangular cuts at its edges and sizes shown at the top of Fig. 11.

The total length of the irregular waveguide was 6 mm and the length of the narrow waveguide with the MC was 5 mm. Magnetostatic waves were excited by microstrip antennas of spin waves 30 μm in width and 3 mm in length. The input antenna was located in the broad part of the irregular waveguide at a distance of 1.5 mm from the plane corresponding to the beginning of a periodic structure in the narrow waveguide. The output antenna was located in the narrow part of the waveguide at the distance $h = 5$ mm from the input antenna. The waveguide with the MC was placed into an external homogeneous magnetic field $H_0 = 440$ Oe oriented

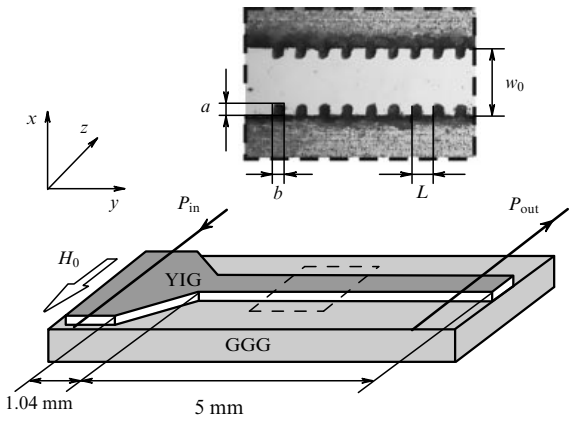

Figure 11. Irregular waveguide with a periodically variable width (1D MC). At the top of the figure is presented a photograph of a part of the structure with dimensions $a = 60$ μm, $b = 60$ μm, $L = 122$ μm, and $w_0 = 353$ μm.

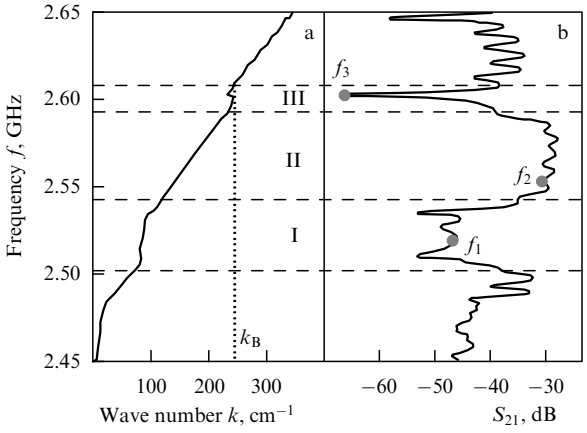

Figure 12. (a) Dispersion characteristic of an MSSW and (b) the corresponding dependence of the transmission coefficient S_{21} on frequency. Grey circles indicate characteristic frequencies at which measurements were performed: $f_1 = 2.519$ GHz, $f_2 = 2.55$ GHz, $f_3 = 2.608$ GHz.

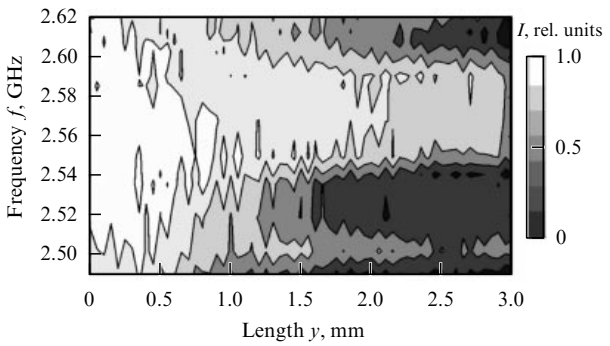

Figure 13. Spatial frequency distribution of the MSW intensity $I(y, f)$ in an MC.

in the waveguide plane along the axis of the antennas. In the irregular waveguide with the MC, surface MSWs were excited.

The elements of the scattering matrix of the MC (S parameters) were measured in the microwave range with a vector circuit analyzer. Figure 12 shows the results of measuring the S parameters of the MC for the input microwave signal power $P_{in} = -30$ dB to exclude the influence of three-magnon decay processes of spin waves. The dispersion characteristic of MSWs (Fig. 12a) was found from the measured phase incursion $\varphi(f)$ of the MSW between microstrip antennas in accordance with the relation $k(f) = \varphi(f)/h$. Figure 12b presents the results of measurements of the frequency transmission coefficient $S_{21}(f)$.

The dependence $S_{21}(f)$ contains three characteristic frequency regions with different MSW attenuation levels. Region I, with the strong attenuation level -50 dB, is located near the beginning of the MSW spectrum with wave numbers $k \approx 100$ cm^{-1}. Region III, with the central frequency $f_3 = 2.608$ GHz and attenuation level -60 dB, corresponds to MSWs with the wave number $k \approx 240$ cm^{-1}. Regions I and III are separated by region II, in which MSWs propagate with a relatively weak attenuation ($S_{12} \approx -30$ dB). The measurement of the dispersion characteristic of the MC shows that region III corresponds to MSWs with wave numbers close to the wave number k_B of the first Bragg forbidden band, $k \approx k_B = \pi/L = 257$ cm^{-1}. The mechanism of the appearance of region I with strong attenuation is caused by the multimode composition of propagating MSWs.

The spatial distribution of the MSW intensity in the MC at different frequencies upon excitation by 200 ns microwave pulses with the pulse repetition period $T_i = 1.5$ μs and different powers was studied by the MBS method. The irregular waveguide was scanned with a different spatial resolution, $\Delta y \Delta z = 0.05 \times 0.03$ mm. The intensity of light scattered by spin waves was determined from the relation $I(y, z, t) \propto |m(y, z, t)|^2$, where $m(y, z, t)$ is the MSW amplitude.

Figure 13 shows the space–frequency distribution of the integrated intensity

$$\frac{I(f, y)}{I_0(f)} = \int_0^{T_i} \int_0^{w_0} \frac{I(f, y, z, t)}{I_0(f)} \, dz \, dt ,$$

where $I_0(f)$ is the integrated intensity measured in the cross section $y = 0$ at a specified frequency f. We note that the onset of the MC in the narrow waveguide corresponds to the coordinate $y_{MC} = 0.25$ mm. Figure 13 demonstrates two frequency regions with strong spatial MSW attenuation, the positions of these regions at the frequency scale corresponding to regions I and III in Fig. 12b. Forbidden bands are formed in this case at a distance of about 1 mm from the MC, which fits about 10 periods of the structure. Thus, the spatial formation of forbidden bands occurs due to the scattering of MSWs by the periodic edges of the waveguide.

The spatial distribution of spin waves in an MC is characterized by the integrated intensity

$$I(y, z) = \int_0^{T_i} I(y, z, t) \, dt .$$

The distribution $I(y, z)$ showed that MSW modes with the transverse amplitude distribution $\sin(n\pi z/w_0)$, $n = 1, 3, \ldots$, propagate at all frequencies in the regular part of the narrow waveguide up to the beginning of the MC ($y < y_{MC}$). The main contribution to the formation of the spatial intensity distribution of spin waves is introduced by modes with $n = 1$ and 3. In the waveguide under study, the regime of multimode excitation and propagation of MSWs in the MC is realized [82].

Figures 14a–c show spatial distributions of the integrated intensity $I(y, z)$ of MSWs measured at frequencies f_1, f_2, and f_3. The transverse intensity distributions in the broad and narrow parts of the waveguide (in the cross sections $y = 0.70$ and 0.76 mm) are shown in the right part of the figure.

At all frequencies in the MC region, a regular spatial MSW intensity distribution is formed due to the superposition of incident and scattered modes with different mode indices n. The intensity distribution is almost symmetric with respect to the longitudinal MC axis, i.e., n takes odd values.

We note that the mode composition of propagating MSWs can be controlled by changing the waveguide width: the axial symmetry breaking of the structure leads to the formation of even width modes. However, if the axial symmetry is preserved as the film waveguide width changes, the mode composition of propagating MSWs remains invariable.

We first consider regions I and III, corresponding to the forbidden bands (Figs 14a, c). We introduce the coefficient of reflection of the wave with a number n from one period of the MC, $\Gamma_n = (k_{0n} - k_{1n})/(k_{0n} + k_{1n})$, where k_{0n} and k_{1n} are the wave numbers of the MSW at the frequency f with the

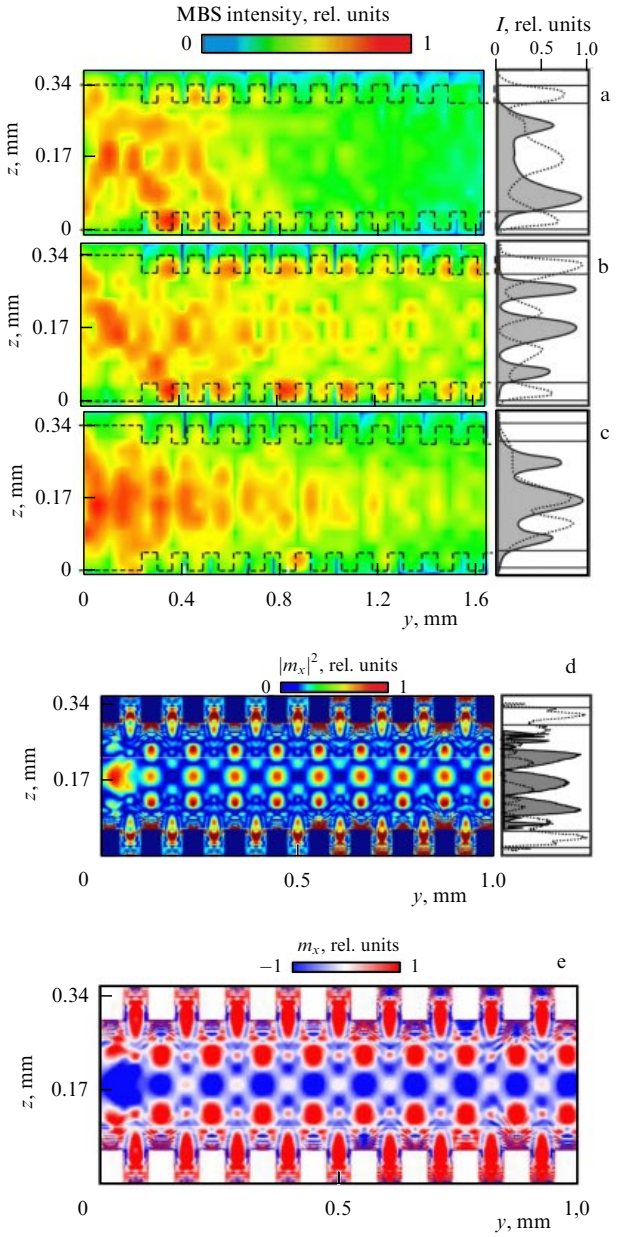

Figure 14. (Color online.) Spatial distribution $I(y, z)$ of MSWs in an MC at different input signal frequencies (a) f_1, (b) f_2, and (c) f_3 and transverse distributions $I(z)$ in the broad ($y = 0.70$ mm, dotted curve) and narrow ($y = 0.76$ mm, solid curve) parts of the waveguide. (d) Spatial distributions of the component m_x squared and (e) the component m_x of the spin-wave magnetization obtained by numerical simulations. The input signal frequency is $f = 2.55$ GHz, the permanent magnetic field strength is $H_0 = 440$ Oe.

number n in the waveguide with respective widths w_0 and $w_1 = w_0 - 2a$. The estimates of Γ_n for the MC under study performed by the dispersion characteristics of MSWs for width-restricted waveguides [76, 77] show that the spatial modulation of waveguide edges in region I (Fig. 14a) cannot be considered small. The spatial intensity distribution essentially depends on the intermode coupling of waves with different indices n and their scattering from waveguide boundaries. These mechanisms cause a rapid spatial decay of MSWs and the formation of a broad forbidden band.

In frequency region III (Fig. 14c), the reflection coefficient Γ_n decreases, and the MSW intensity is redistributed from the MC edges to its longitudinal axis. The efficiency of MSW scattering from periodical waveguide edges decreases; during wave propagation, the profile of the transverse intensity distribution $I(y, z)$ approaches the distribution $\sin^2(\pi z/w_0)$ for the fundamental mode, and a forbidden Bragg band is realized.

In frequency region II (Fig. 14b), MSWs propagate with a weak decay, and the transverse intensity distribution is multimode.

We note that as the signal frequency increases from f_1 to f_3, the transverse MSW intensity distribution $I(z)$ in the waveguide transforms such that the number and positions of maxima change with respect to the longitudinal axis of the waveguide, i.e., the mode composition of propagating waves changes.

Figures 14d, e show the numerically calculated characteristics of a spin wave propagating in a YIG waveguide with periodically modulated boundaries for the input signal frequency 2.5 GHz. The numerical simulation was performed by solving the Landau–Lifshitz–Gilbert equation by the FDTD method [55]. The decay parameter for the Landau–Lifshitz–Gilbert equation was set equal to $\alpha = 5 \times 10^{-5}$ [83, 84]. The exchange constant for the YIG film was $A_{ex} = 3.614 \times 10^{-12}$ J m^{-1}. The amplitude of the dynamic magnetization component in the excitation region (at the left boundary of the calculation region) $B_{ext} = 10^{-7}$ T was below the nonlinear effect threshold [36]. Numerical simulation was performed by specifying a region with a continuously increasing decay parameter near the right boundary of the calculation region to reduce the influence of the reflected spin wave on the signal propagation dynamics in the YIG waveguide.

Color in Fig. 14d shows the distribution $|m_x|^2$ in the calculation region in the established regime for $t = 250$ ns. The type of the distribution $|m_x|^2$ is in good agreement with experimental results (Fig. 14b). The dependences $|m_x|^2$ are presented in the broad and narrow parts of the irregular waveguide. Three maxima in the transverse distribution $|m_x|^2$ can be identified in the narrow region (233 μm in width) and four maxima in the broad region (353 μm in width).

Thus, the features of the multimode propagation of MSWs in an irregular YIG waveguide with a periodically modulated width formed from a YIG film by laser scribing were studied by the MBS method in magnetic materials. It was shown that the mode composition of propagating MSWs can be controlled by varying the waveguide width. Breaking the axial symmetry of the structure leads to the formation of even width modes. If the axial symmetry is preserved when changing the width of the film waveguide, the mode composition of propagating MSWs does not change.

The mode composition of an MSW propagating in an irregular waveguide was determined in a numerical experiment. The forbidden band in the low-frequency region is formed due to the intermode interaction of MSWs. The second nontransmission band corresponds to the forbidden Bragg band of an MC with a weakly periodically modulated boundary. The mode interaction effects should be taken into account in the construction of mathematical models of one-dimensional MCs and the fabrication of frequency-selective devices based on them.

3.2 Lumped systems (resonators)

3.2.1 Defect modes. One important problem in practical applications of MCs is the relation of parameters of forbidden bands in the spectrum of spin waves to different

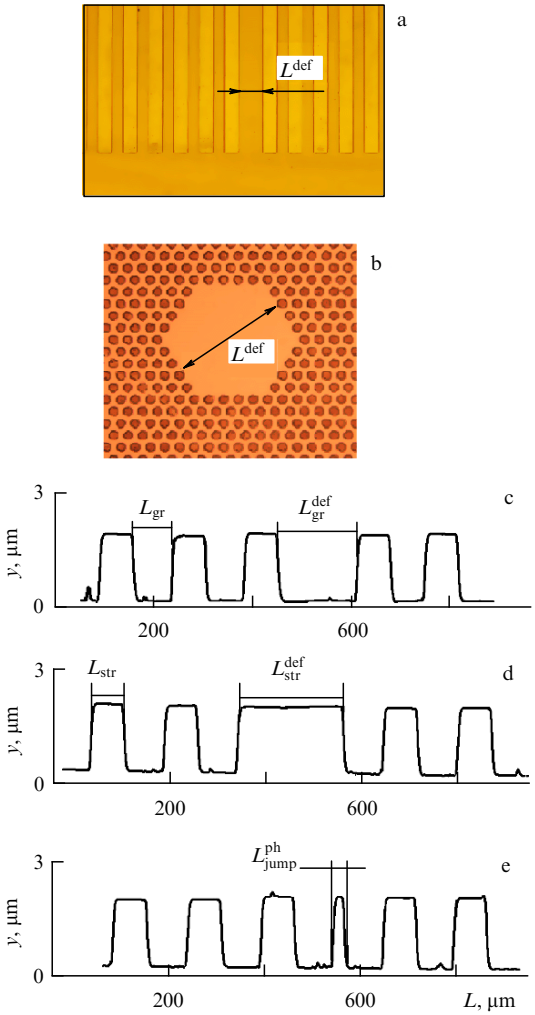

Figure 15. Photographs of the surface of a (a) one-dimensional and (b) two-dimensional MC. Surface profiles of an MC with periodic-structure defects in the form of (c) a groove ($L_{\text{gr}}^{\text{def}}$), (d) a strip ($L_{\text{str}}^{\text{def}}$), and (e) a phase jump ($L_{\text{jump}}^{\text{ph}}$).

types of imperfections of a periodic structure, which can be purposely produced or appear randomly for technological reasons. The theoretical consideration of MC properties whose periodicity is violated by random variations in MC parameters [85]; the modulation of not one but a few parameters [86]; the inhomogeneity of the distribution of dissipative parameters [87]; and the quality, profile, and finite thickness of boundaries between MC regions with different magnetic parameters [88, 89] have shown that these factors affect the width of nontransmission bands. It was also shown theoretically that a local change in the thickness of one of the layers in a one-dimensional MC leads to the appearance of discrete levels in the nontransmission band at frequencies corresponding to the spin wave length that is a multiple of the doubled thickness of the defect layer [72, 90, 91]. Defect modes have been experimentally observed for both one-dimensional [92] and two-dimensional [93] MCs with structural defects.

Figure 15 shows photographs of defect regions and surface profiles for such crystals. As a whole, the conditions of defect mode formation are consistent with the excitation conditions of Bragg resonators [94] relating the wavelength to the characteristic size of the defect region in the wave propagation direction.

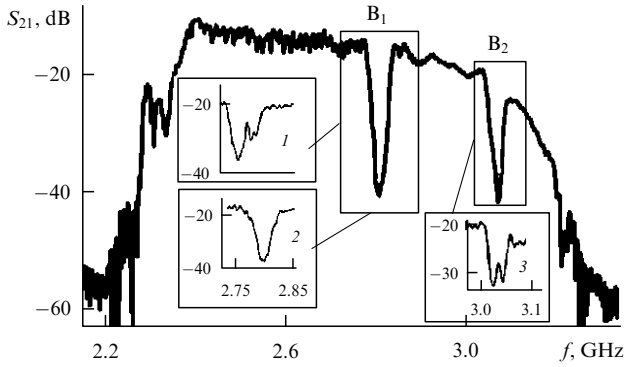

Figure 16. Dependence $S_{21}(f)$ for the propagation of magnetostatic surface spin waves in a defect-free region of a 1D MC (a 14.7 μm thick YIG film, $\Lambda = 150$ μm, the groove width and depth are 80 μm and 1.8 μm). Insets *1* and *2* show the respective shape of the B_1 band for the defect strip ($L_{\text{str}}^{\text{def}} = 150$ μm) and defect groove ($L_{\text{gr}}^{\text{def}} = 225$ μm) located between converters. Inset *3* shows the shape of the B_2 band for the phase jump defect, $H = 320$ Oe.

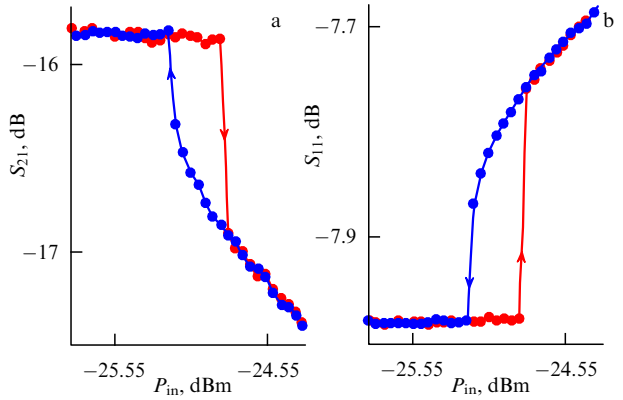

Figure 17. Dependences of (a) the transmission coefficient S_{21} and (b) the reflection coefficient S_{11} on the pump power during the propagation of magnetostatic surface spin waves in a 2D MC (a 14.7 μm thick YIG film, a hexagonal lattice of pits 75 μm in diameter and 1.4 μm in depth with a period of 150 μm) with a defect in the form of the absence of 18 lattice periods at the defect mode frequency 2637 MHz for $H = 290$ Oe.

Figure 16 shows the typical transfer spectrum $S_{21}(f)$ of the model delay line for spin waves based on a one-dimensional defect-free MC. When the longitudinal size L^{def} of the defect is a multiple of the period Λ of the surface structure, defect modes are manifested in the form of a reduction in spin wave losses (with respect to losses in a defect-free MC) in a narrow frequency region within the nontransmission B_1 band (see inset *1* in Fig. 16) and less distinctly in the B_2 band. We note that the type of defect (groove or cusp, Figs 15c, d) does not significantly affect the position of the defect mode. At the same time, in the case of a 'phase jump' structural defect (Fig. 15e), the defect mode appears only in the B_2 band (see the inset *3* in Fig. 16).

It has been shown that under parametric instability conditions, defect modes demonstrate bistability [95], which is manifested in the ambiguity of the dependence of the transmission $S_{21}(f)$ and reflection $S_{11}(f)$ coefficients on the change in the input signal power P_{in} (Fig. 17). In this case, the thresholds of the parametric instability and bistability at the defect mode frequency are lower than the thresholds of

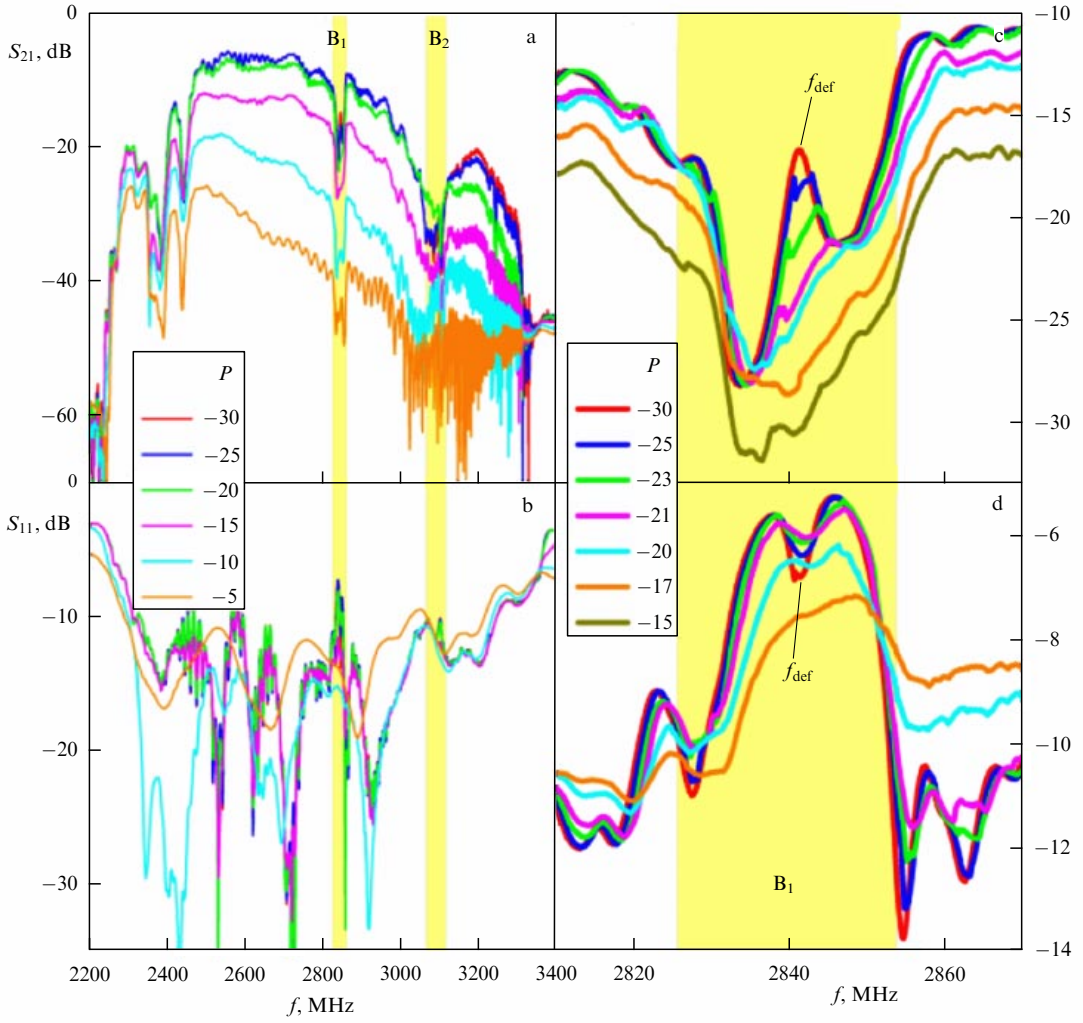

Figure 18. (Color online.) Dependences of (a, c) the transmission coefficient $S_{21}(f)$ and (b, d) the reflection coefficient $S_{11}(f)$ in a 2D MC (with the parameters presented in Fig. 17) for different input power levels P (in dBm). $H = 312$ Oe.

the parametric instability of spin waves in the MC at all other frequencies, which demonstrates the field amplification at the defect mode. We note that the defect mode does not appear upon increasing the pump supercriticality (Fig. 18), and Bragg resonances disappear as the pump power increases further [96].

3.2.2 Finite array of oscillators. The study of diverse magnetic micro- and nanostructures for applications in spintronics and magnetic logic is attracting considerable attention [8, 9, 97–101]. The magnetization dynamics of such structures depend on the parameters of an MC representing a 'transmitting' medium for a spin wave. Such magnonic crystals [102, 103] can be formed, for example, by the introduction of periodic structures such as magnetic dots, strips, and dielectric inclusions [2, 104–106].

The problem of spin wave scattering by an infinite system of magnetic and nonmagnetic cylindrical inclusions was studied in [43, 107–113]. In particular, it was shown that under certain conditions, at inclusion boundaries, edge spin waves are excited that have a propagation nonreciprocity with respect to an external magnetic field and magnetization direction (Fig. 19). It was predicted that edge spin waves can exist in different magnetic structures, such as ferromagnetic islets, discs and rings, and semi-infinite systems of dipole-bounded magnetic columns [114–118]. In these papers, systems with infinite or semi-infinite perturbations were considered and therefore the study of the properties of systems for spatially bounded perturbations is of special interest.

This section is devoted to a theoretical study of the propagation of a direct bulk magnetostatic wave [36] in a metallized ferromagnetic plate (matrix) containing an array of a finite number of ferromagnetic cylindrical inclusions [42]. We consider a ferromagnetic matrix of thickness d with a saturation magnetization M_s^0 (see Fig. 2). Cylindrical inclusions of radius R consist of a ferromagnetic material with a saturation magnetization M_s^1. An external magnetic field H_{ext} is applied along the z axis normally to the matrix.

The solution is obtained by the multiple scattering method described in Section 2.2.1. The distribution of the real part of the magnetostatic potential of a spin wave scattered by the system of inclusions shown in Fig. 20 depends on the wave parameter $k_r^0 R_{12}$ and the size of the inclusion cluster. For the small wave parameter $k_r^0 R_{12} \lesssim \pi$, the distribution has the form of a spiral (Fig. 20a). For the large wave parameter $k_r^0 R_{12} \gtrsim \pi$ (Fig. 20b), Bragg interference between potentials scattered by different inclusions is manifested. The spiral type of the potential distribution of the scattered spin wave in Fig. 20 is observed due to the

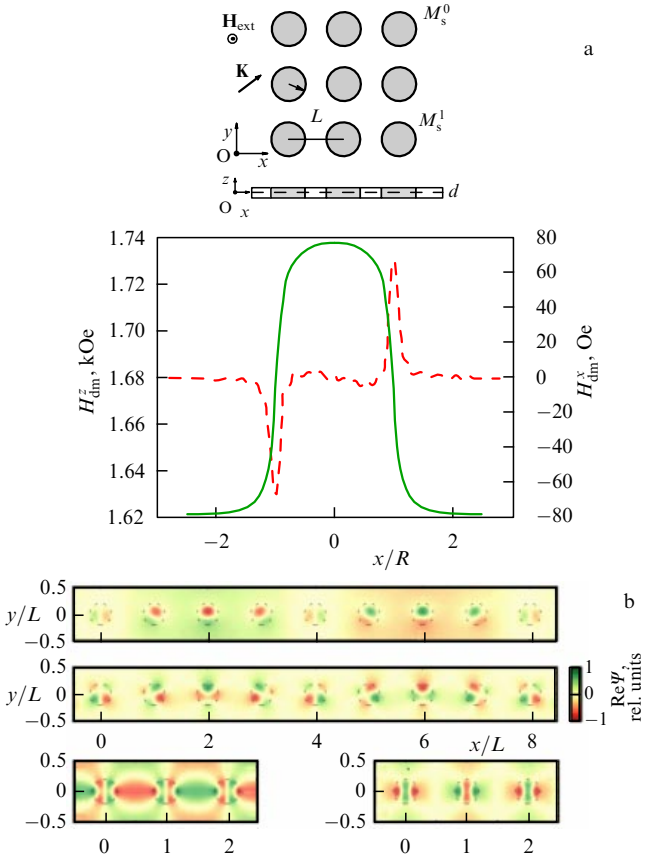

Figure 19. (Color online.) (a) Diagram of the MC under study and the demagnetization field profile in it. (b) The distribution of the real part of the magnetostatic potential of a spin wave exciting asymmetric local rotational modes [43].

antisymmetry of the magnetic permeability tensor $\overleftrightarrow{\mu}(\omega)$ of the ferromagnet, manifested in a violation of the reciprocity of the scattering matrix, $T_m(\omega) \neq T_{-m}(\omega)$, of an isolated inclusion. Omitting cumbersome calculations, the expression for the component of the magnetic potential $\Psi_{kj}^{\text{scat}}(r_j, \phi_j)$ of the scattered spin wave can be written in the convenient form

$$\Psi_{kj}^{\text{scat}}(r_j, \phi_j) \approx \frac{1}{4}\,\varepsilon^{(k)} U_j^{(k)} H_1(k_r^0 r_j) \times \left(\Psi_k^{\text{scat(c)}} \cos\phi_j + \Psi_k^{\text{scat(s)}} \sin\phi_j\right), \tag{24}$$

where the amplitudes at the cosine and sine are

$$\Psi_k^{\text{scat(c)}} = \mathrm{i}\left(\frac{T_1}{\lambda_k^{(1)}} + \frac{T_{-1}}{\lambda_k^{(-1)}}\right)$$
$$\Psi_k^{\text{scat(s)}} = -\left(\frac{T_1}{\lambda_k^{(1)}} - \frac{T_{-1}}{\lambda_k^{(-1)}}\right). \tag{25}$$

The spiral form of the potential distribution for the scattered spin wave is mainly determined by the sine amplitude. This is most clearly manifested in the scattering of a spin wave by one isolated inclusion when the sine amplitude is proportional to the difference $T_1 - T_{-1}$.

A study of the frequency characteristics of four circularly arranged inclusions shows that the amplitude $1/\lambda_k^{(m)}$ of the kth eigenmode can have several resonances with frequencies and Q factors that can greatly depend on the inclusion cluster radius for closely or almost closely packed inclusions in the cluster. Such resonance features make the circular cluster of four ferromagnetic inclusions inside the ferromagnetic matrix a specific Fabry–Perot interferometer for filtering spin waves. The resonance behavior of $\text{Re}\,(1/\lambda_4^{(-1)})$ for the inclusion radius $R = 1.8$ μm and two distances between nearest inclusions $R_{12} = 6.2$ and 6.6 μm is shown in Fig. 21a. Figure 21b shows the dependence of the resonance Q factor on the distance R_{12} between nearest inclusions, reaching the maximum value $Q = 10^6$ for $R = 1.8$ μm and $R_{12} = 5.9$ μm. For comparison, we note that the peak value of the resonance Q factor for $U^{(4)}$ with the multipole index $m = 0$ is $Q = 5000$.

In this section, we have presented theoretical calculations of the multiple scattering of a magnetostatic spin wave propagating in a metalized ferromagnetic film with a finite number of cylindrical ferromagnetic inclusions. We restricted ourselves to the case where the external magnetic field is perpendicular to the surface of the metalized matrix film and the saturation magnetizations of the matrix and inclusion are different. The multiple scattering method can be applied to

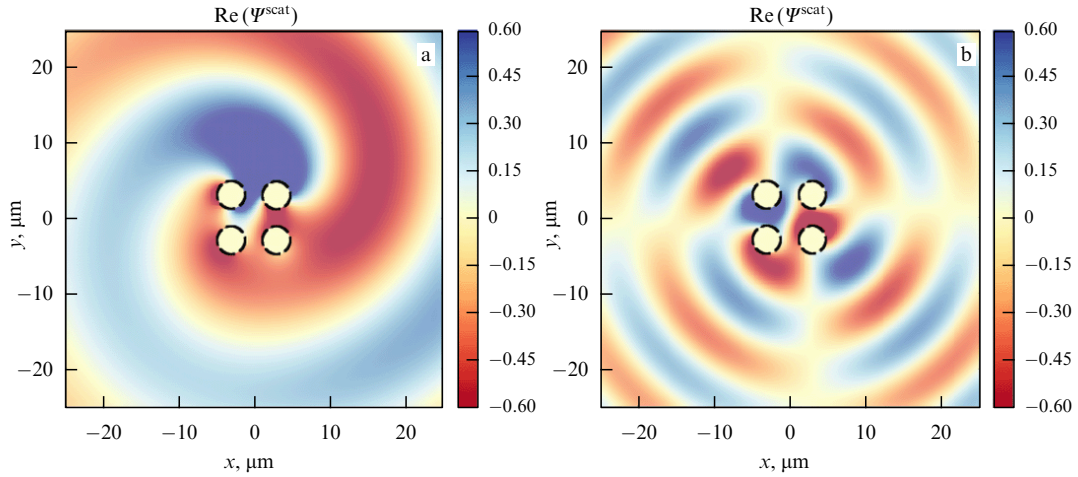

Figure 20. (Color online.) Helical distribution of the real part of the total magnetostatic potential of a spin wave scattered by four inclusions for wave parameters (a) $k_r^0 R_{12} = 2.1$ and (b) $k_r^0 R_{12} = 4.3$.

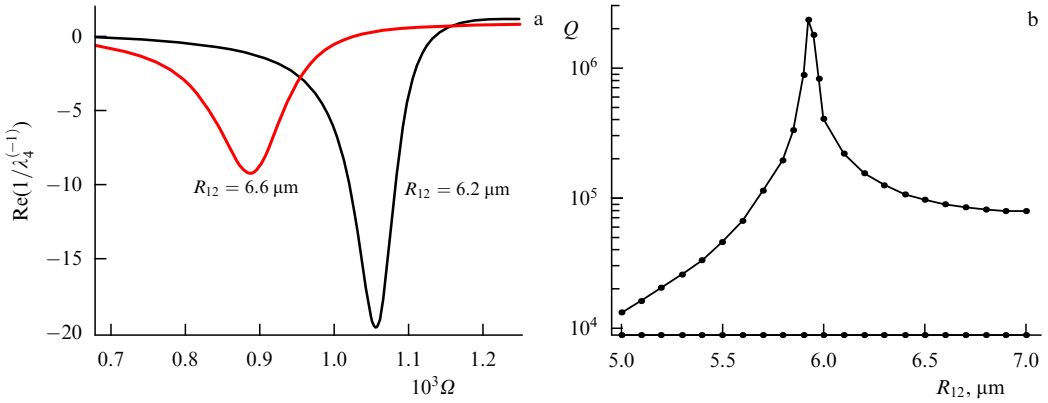

Figure 21. (a) Dependence of $\mathrm{Re}\,(1/\lambda_4^{(-1)})$ on the normalized frequency $\Omega = \omega/\omega_{H_0} - 1$ (where ω_{H_0} is the ferromagnetic resonance frequency in the matrix) in a closely packed system of inclusions with parameters $R_{12} = 6.2$ μm (narrower peak) and $R_{12} = 6.6$ μm (broader peak) with the inclusion radius $R = 1.8$ μm. (b) The peak quality parameter Q as a function of the distance R_{12} between cylinders.

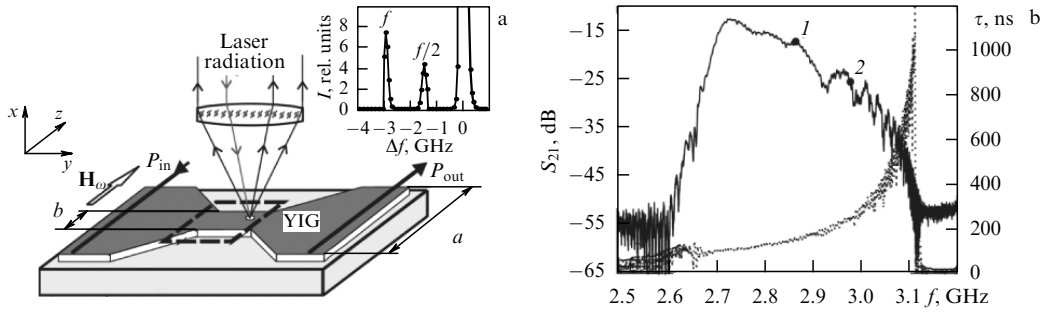

Figure 22. (a) Waveguide under study ($a = 1.97$ mm, $b = 0.25$ mm) and a schematic of the experiment. The inset shows the MBS spectrum obtained at a point inside the narrow waveguide. (b) Frequency dependences of the transmission coefficient S_{21} (solid curve) and the group delay time τ (dotted curve) of the MSSW ($P_{\mathrm{in}} = -30$ dBmW).

arbitrarily arranged inclusions of arbitrary sizes. The analytic solution obtained for four identical inclusions with the centers arranged periodically along a circle showed the presence of eigenmodes of the Bloch wave type with the Q factor reaching 10^6, which makes this structure a Fabry–Perot interferometer filter for spin waves. The theory can be extended to other types of inclusions, for example, metal or dielectric ones.

3.3 Irregular waveguide systems

Planar waveguide systems based on thin YIG films are used as base elements in diverse devices of functional magnetoelectronics [7]. At present, the space–time dynamics of magnetization waves, the three-magnon decay processes of magnetostatic waves, and the parametric excitation of spin waves are being extensively studied by MBS spectroscopy [15, 119, 120]. However, the dynamics of these processes in longitudinally irregular transversely restricted structures have not been studied so far. This section is devoted to MBS studies of the excitation of surface MSWs in such structures.

For these studies, we developed a planar longitudinally irregular ferrite waveguide (Fig. 22a) consisting of two longitudinally regular waveguides with different widths connected with each other via matching regions with linearly changing widths. The waveguide was fabricated by the laser scribing method from a 10 μm thick YIG film with the saturation magnetization $4\pi M_0 = 1350$ G. MSSWs were excited with two parallel 0.25 mm thick microstrip antennas (MSAs) 4 mm in length and 30 μm in width separated by 5 mm on an Al_2O_3 substrate. The waveguide was placed above MSAs such that the antennas were in broad parts of the waveguide at a distance of 1 mm from narrow regions. This structure was placed in an external homogeneous magnetic field $H_0 = 490$ Oe. The waveguide dimensions, the coordinate system, and the mutual orientation of the magnetic field and MSAs are shown in Fig. 22a. Microwave pulses 200 ns in duration with the power P_{in} and the carrier frequency f were supplied to the input MSA. To avoid waveguide heating by the microwave signal, the pulse repetition period was 1 μs. The components of the scattering matrix of the waveguide and the frequency dependences of the group delay time of the MSSWs were measured with a microwave circuit analyzer.

The choice of a longitudinally irregular waveguide and the placement of the antennas in broad parts of the waveguide were made with the aim of spatially separating two parametric SW excitation processes: excitation of SWs at the frequency $f/2$ by fields of the input MSA and excitation of SWs during three-magnon MSSW decay processes. For spatially inhomogeneous pump fields, the development of parametric processes is determined by the threshold power density W_{th} of the MSSW [36] in a given waveguide region. For an irregular waveguide, the power density W at a fixed input power P_{in} and excitation of MSSWs in its broad part increase during the propagation of MSSWs from the broad waveguide to the narrow one (in the absence of wave decay).

The space–time distribution of the amplitude of high-frequency magnetizations $m(t, y, z)$ of MSSWs and SWs at different frequencies was studied by the MBS method. The waveguide surface was scanned by a focused laser beam with

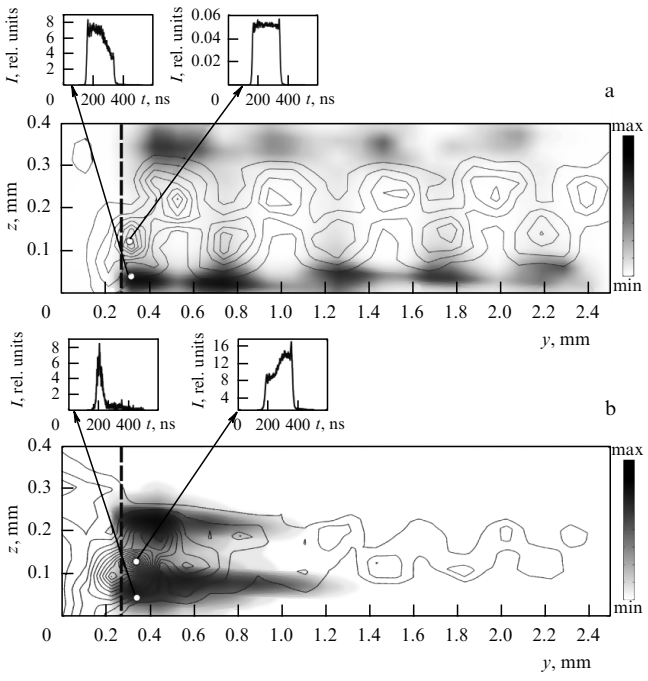

Figure 23. Spatial distributions $I(y,z)$ in a longitudinally irregular waveguide at the frequencies (a) $f = 2.872$ GHz and (b) $f = 2.981$ GHz. $P_{in} = 0$ dBmW, MSSWs are lines of equal intensity, SWs are regions with the gradient filling. The dependences $I(t)$ correspond to the indicated light circles of the waveguide.

the diameter 20–30 μm and the spectrum and intensity of inelastically scattered light $I(t,y,z) \sim |\mathbf{m}(t,y,z)|^2$ were measured [15]. The scan was performed with a step of 0.1 mm along the y axis (24 points) and a step of 0.03 mm along the z axis (13 points). Figure 22a shows a schematic of the MBS method, the scan region (dashed lines), and the scattering spectrum containing only the Stokes component (inset).

Figure 22b presents the frequency dependences of the transmission coefficient S_{21} and the group delay time τ of the MSSW for the power P_{in} considerably lower than the three-magnon decay threshold. The MSSW was excited in the frequency range from $f_\perp = \gamma\sqrt{H_0(H_0 + 4\pi M_0)} = 2.66$ GHz to $f_m = \gamma(H_0 + 2\pi M_0) = 3.26$ GHz, where $\gamma = 2.8$ GHz kOe^{-1} is the gyromagnetic ratio. The low signal decay level (−13 dB) and the absence of resonance peaks demonstrate good matching between parts of the longitudinally irregular waveguide. Numbers *1* and *2* in the dependence S_{21} indicate frequencies f at which further measurements were performed [$f = 2.872$ GHz (*1*) and $f = 2.981$ GHz (*2*)].

Figure 23 shows the spatial distributions of the light intensity $I(y,z) = \int_0^T I(t,y,z)\,dt$ obtained by combining the results of measurements at frequencies f (MSSW) and $f/2$ (SW). The dashed straight line indicates the narrow waveguide onset.

In the narrow regular waveguide at a frequency f, the magnetization $m(t,y,z)$ is the superposition of n MSSW modes with wave numbers k_n and amplitudes depending on z as $\alpha_n(z) = A_n \sin(n\pi z/b)$, where A_n is a coefficient determined by the excitation field configuration at the input of the narrow waveguide [121, 122]. An analysis of the experimental spatial intensity distribution at the frequency $f = 2.872$ GHz (Fig. 23a) showed that it corresponds to the superposition of MSSW modes with $n = 1$ and 2 and the beat length $L = 0.55$ mm. The calculation of eigenmodes and the corresponding wave numbers [121] for a uniformly magnetized narrow regular waveguide gave the values of wave numbers 260 and 378 cm^{-1} and the beat length $L = 2\pi/|k_1 - k_2| = 0.56$ mm, in good agreement with experimental results.

The spatial distribution $I(y,z)$ for parametrically excited SWs at the frequency $f/2$ is shown in Fig. 23a. For $P_{in} = 0$, the power density W does not exceed the threshold in the region to the left of the narrow waveguide input, and the SWs are not excited. Inside the narrow waveguide, the SWs are excited near its side boundaries, and the maxima of the spatial distribution of the SWs do not coincide with the maxima of the spatial distribution of the MSSWs. At the top of Fig. 23a, the time dependences $I(t)$ at a frequency f are shown as obtained at two spatial points: in the region of the local maximum of the spatial MSSW distribution and in the region of the local maximum of the SW spatial distribution (near the waveguide edge). We can see that for a given input power and microwave pulse duration, a characteristic 'chip' in the time dependence is observed only in the spatial SW excitation region.

In our opinion, this effect is explained by the following factors. For a broad ferrite film ($d/b \ll 1$) magnetized with an external magnetic film H_0 along the z axis, the internal magnetic field H_i coincides with H_0 and is homogeneous. As the ratio d/b increases, the inhomogeneity of H_i near the waveguide edges should be taken into account. The size Δ of the spatial region along the z axis, where the magnetic field H_i depends on z and considerably decreases toward the waveguide edges, can be estimated from the solution of the corresponding magnetostatic problem [123]. For the ratio $d/b = 0.04$, the estimate gives $\Delta \approx 25$ μm. The size of these regions is small compared with the narrow waveguide width ($2\Delta/b \ll 1$), and they hardly affect the characteristics of the MSSW modes. For SWs propagating along the z axis with the wave number $k = 10^4$ cm^{-1} [119], the condition $k\Delta \ll 1$ is satisfied, and the dispersion characteristics and boundary frequencies of the SW spectrum are determined by the magnetic field strength $H_i(z)$ at the given spatial point. In this spatial region, the boundary frequencies of the SW spectrum shift to lower frequencies with respect to the boundary frequencies in the rest of the narrow waveguide, where $H_i = H_0$. This leads to a decrease in the wave numbers k of SWs at the frequency $f/2$, a decrease in their decay, and therefore to a reduction in the threshold power densities W_{th} [36] of three-magnon MSSW decay processes near the edges of the narrow waveguide.

The spatial magnetization distribution at the frequency $f = 2.981$ GHz (Fig. 23b) for $y > 1.4$ mm corresponds to an superposition of MSSW modes with $n = 1$ and 2 and the beat length $L = 0.4$ mm. At the onset of the narrow waveguide (0.2 mm $< y <$ 1.4 mm), a region is observed in which the magnetization distribution has a more complicated character. The calculation of wave numbers gives $k_1 = 411$ cm^{-1}, $k_2 = 535$ cm^{-1}, and the beat length $L = 0.5$ mm. A shift of the spatial magnetization distribution to the longitudinal axis of the waveguide is observed. For $y < 1/4$ mm, the MSSW experiences an additional nonlinear decay due to three-magnon decay processes. In the spatial distribution of SWs at the frequency $f/2$, the two spatial regions of efficient SW excitation are displaced from the waveguide edges to its longitudinal axis. The local SW maxima do not coincide with the local maxima of the MSSW distribution either. At the top of Fig. 23b, the dependences $I(t)$ at the frequency f

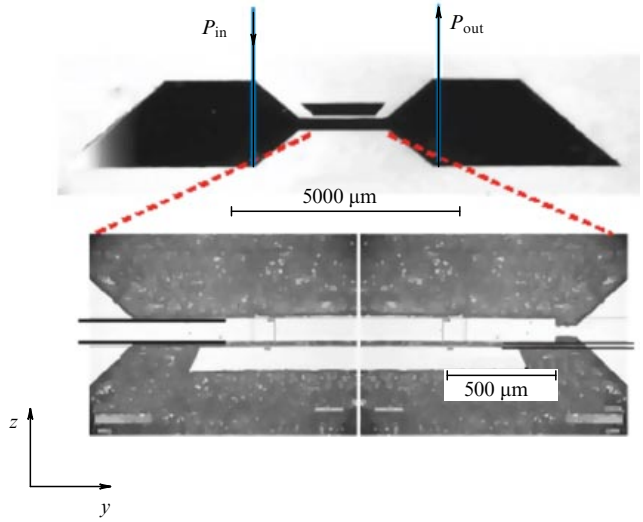

Figure 24. System of two laterally coupled ferrite waveguides.

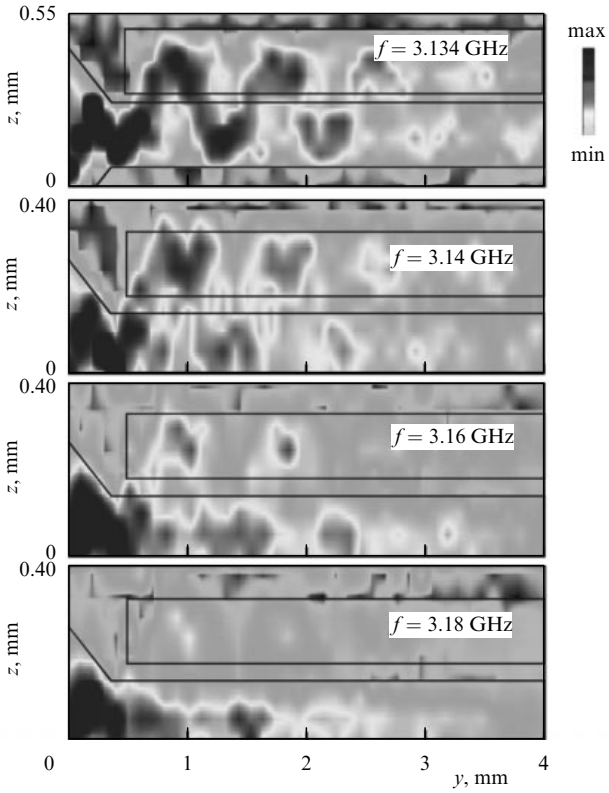

Figure 25. Spatial distributions of the magnetization squared measured by MBS spectroscopy of magnetic materials in a system of two laterally coupled ferrite waveguides for different input signal frequencies shown in the figure.

are shown for two spatial points chosen as described above. We can see that at a point near the waveguide edge, the three-magnon MSSW decay also proceeds at lower threshold power densities. For $y < 1.4$ mm, the MSSW power density is below the threshold at any waveguide point, SWs are not excited, and the MSSW propagates with the linear decay.

Thus, the spatial distribution of MSSW and SW magnetizations at different frequencies was obtained by the MBS method. It is shown that in a longitudinally irregular ferrite film waveguide, the MSSW decay at frequencies for which three-magnon decay processes are allowed occurs most efficiently near the narrow waveguide edges, where threshold levels are minimal. The spatial position of local MSSW maxima in a narrow waveguide is determined by the spatial beats of the two lowest modes and the position of SW local maxima is determined by the distribution of the inhomogeneous internal magnetic field $H_i(z)$ of the narrow waveguide.

3.4 Coupled waveguide systems

3.4.1 Laterally coupled waveguides. Coupled planar ferrite waveguides based on thin YIG films are of interest because they can provide the control of propagation characteristics of surface and volume waves propagating in them and exhibit diverse linear and nonlinear phenomena [26]. Coupled YIG-based structures were studied, for example, in [124–126]. The functional processing of microwave signals is performed, in particular, in devices providing data-flow multiplexing and demultiplexing based on different directional couples: waveguide, microstrip, etc. An analogue of such devices in magneto-electronics is given by systems based on two or more laterally coupled ferrite waveguides. The main parameters of couplers are the frequency range, the power transfer coefficient, and the coupling strength. Below, we consider the state of laterally coupled YIG waveguides in a structure [127] that can be used as a base element for different magneto-electronic devices controlled by the external permanent magnetic field: waveguides, filters, and couplers [7].

The structure shown in Fig. 24 consists of two coupled 10 μm thick YIG waveguides on a 500 μm thick GGG substrate. The width of each of the waveguides separated by the distance $d = 40$ μm is $a = 200$ μm. We considered the excitation and propagation of an MSSW in the film along the z axis. The external magnetic field oriented along the positive direction of the y axis was 600 Oe.

By modifying the method for numerical calculation of electrodynamic characteristics of ferrite structures with a complex cross section [47], we calculated dispersion curves for the first three symmetric and antisymmetric width modes of the structure under study. We studied the dependence of dispersion characteristics on the distance d between the waveguides. For a small change in the parameter d at relatively small absolute values, some discrepancy was observed between dispersion curves in the region of low frequencies and, accordingly, small wave numbers for both symmetric and antisymmetric modes of the coupled ferrite structure. It is shown that as d increases to values comparable to or greater than the width of the waveguides themselves, dispersion characteristics approach those for a single waveguide 200 μm wide. As the frequency increases, the field is more and more localized on the film surface.

The space–time characteristics of the signal propagation through the structure were obtained by Mandelshtam–Brillouin spectroscopy. It has been shown that the signal can be completely transferred from one film to another at frequencies close to the ferromagnetic resonance frequency in the magnetized film (Fig. 25). The results of numerical simulation are in good agreement with experimental data.

3.4.2 Coupled structures based on magnonic crystals. The presence of forbidden bands in the spectrum of spin waves allows the development of MC-based magnetic-field-tunable devices for microwave signal processing and generation [128,

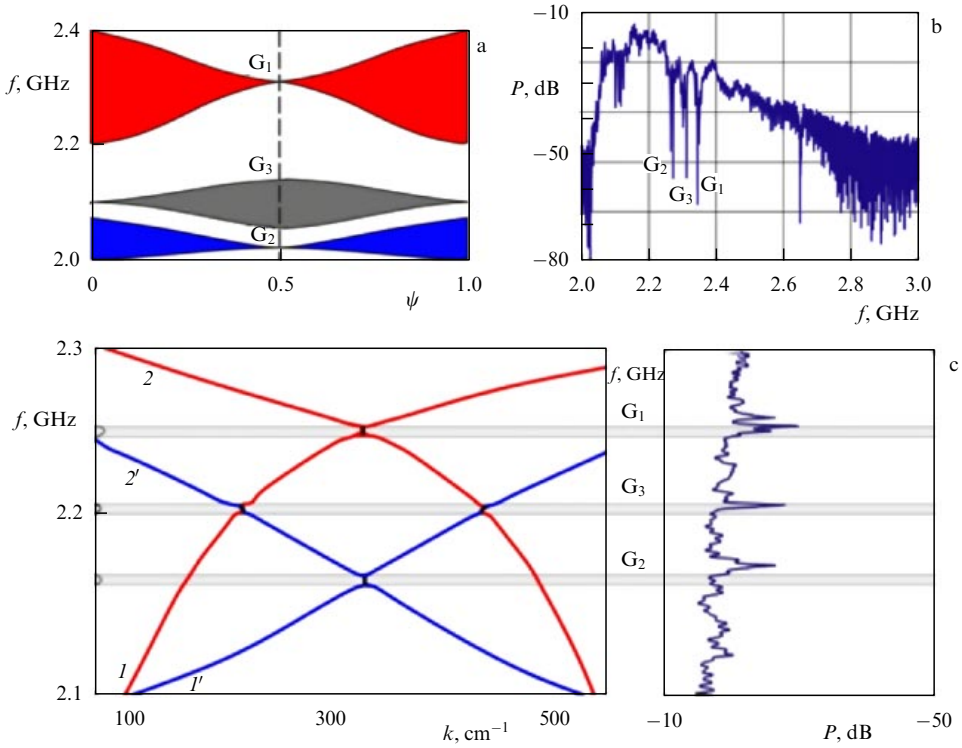

Figure 26. (a) Dependence of the forbidden band width on the shift ψ between MCs. (b) The AFC of the structure obtained with a spectrum analyzer. (c) Dispersion curves of MSWs in the MC–film structure and the experimental AFC of the transmission line.

129]. One efficient method for controlling characteristics of forbidden bands in such devices can be based on the use of periodic structures of coupled magnonic crystals [130, 131]. In the case of two ferromagnetic waveguide structures, their coupling leads to the appearance of fast and slow waves propagating with different group and phase velocities whose characteristics can be controlled by varying the coupling strength [132, 133].

Using the coupled-wave method (see Section 2.2.1), an approach was developed for calculating the dispersion dependences for MSWs in coupled structures such as two magnonic crystals and a magnonic crystal–ferrite film based on wave equations for each MC. As an example, in Fig. 26a, we present the calculated dependences of the width and position of forbidden bands in the MSW spectrum in a structure of two coupled MCs on the phase shift $\psi = (2\pi/L)\Theta$ between MCs in the propagation direction of the waves (L is the structure period and Θ is the shift between periods).

It follows from the results presented in Fig. 26a that for $\psi > 0$, the first Bragg resonance band in the system contains three forbidden bands: G_1, G_2, and G_3. For $0 < \psi < 0.5$, the upper G_1 and lower G_2 forbidden bands narrow with increasing ψ, while the middle band G_3 broadens. In the range $0.5 < \psi < 1$, the upper G_1 and lower G_2 bands broaden, while the middle band G_3 narrows. The widths of G_1 and G_2 achieve their maxima at $\psi = 0$ and 1, while the width of G_3 is maximal at $\psi = 0.5$. The central frequencies of the forbidden bands do not shift.

Figure 26b shows the amplitude–frequency characteristic (AFC) for the MC–MC structure in which periods are displaced with respect to each other. We can see from Fig. 26b that in the frequency range 2.2–2.4 GHz, the AFC exhibits three characteristic decay regions, G_1, G_2, and G_3, corresponding to forbidden bands in Fig. 26a. We note that in the case of a single MC, only one forbidden band exists in this range.

Figure 26c shows dispersion curves calculated using the COMSOL software (at the left of the figure) and the experimental AFC of the coupled MC–ferromagnetic-film structure (at the right of the figure). Curves *1′* and *2′* correspond to slow direct and counter waves, while curves *1* and *2* correspond to fast direct and counter waves. A comparison of numerical simulations with experimental data in Fig. 26c shows that the decay regions in the AFC (at the right of the figure) are in good agreement in frequency with calculations of the central frequencies of forbidden bands G_1, G_2, and G_3. A small discrepancy exists about 20 MHz for the low-frequency band G_3.

Nonlinear effects in the structure of coupled MCs are a set of nonlinear effects in coupled homogeneous films [132, 133] and a single MC. Upon excitation of both normal waves at the forbidden band frequency, the effect of 'double nonlinear switching' occurs. For the pulse amplitude at the MC1 input $A_{01} < A_{n1}$, the pulse is reflected, whereas the pulse with the amplitude $A_{01} > A_{n1}$ propagates through the MC–MC structure (as in the case of a single MC). If $A_{01} < A_{n2}$, this pulse can be transferred to MC2, while for $A_{01} > A_{n2}$, it is not transferred to MC2 and escapes from MC1 (as in the case of coupled homogeneous films) [133, 134]. The values of the amplitudes A_{n1} and A_{n2} corresponding to switching points depend on the coupling parameter in this structure.

The effect of double nonlinear switching observed in coupled MCs can be used for the development of multifunctional devices based on the MC–MC structure. In particular, a communication line containing coupled MCs can operate as a nonlinear directional coupler in which, depending on the input power, the pulse can escape through one of the four ports of the coupled structure (Fig. 27a). Figure 27b shows the transfer characteristics of waves in

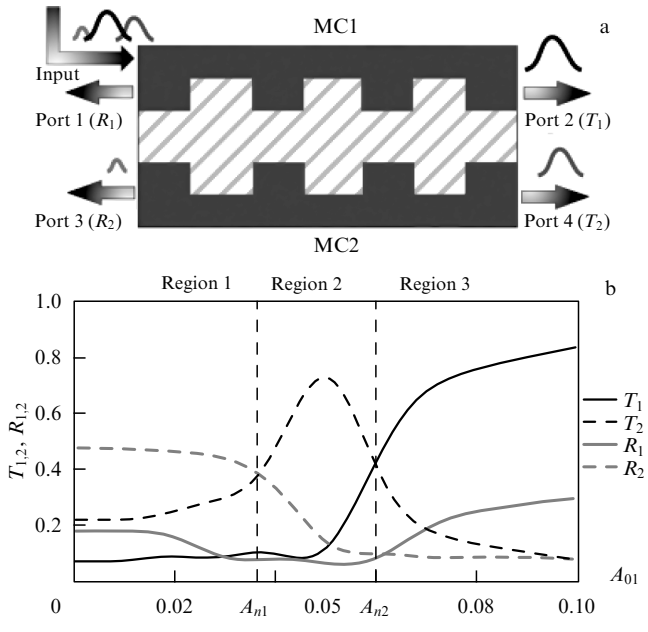

Figure 27. (a) Schematic of an MC–MC nonlinear coupler. $R_{1,2}$ and $T_{1,2}$ are the reflection and transmission coefficients for MC1 and MC2. (b) Transmission characteristics as functions of the input signal amplitude A_{01} in the MC–MC structure for $\eta = 0$.

MC1 and MC2 for a frequency lying at the center of one of the forbidden bands. Three characteristic regions can be distinguished as follows: region 1: most of the power escapes through port 3; region 2: most of the power escapes through port 4; and region 3: most of the power escapes through port 2.

Thus, we showed that the resonance properties of structures based on coupled MCs can be controlled, which can be used for the development of rejection and band filters, filters for separating channels, nonlinear couplers, and multiplexors.

3.5 Controllable magnetic structures

3.5.1 Multiferroid structures based on magnonic crystals and ferroelectrics. Another method for controlling the characteristics of forbidden bands in MCs, along with applying a magnetic field, is the use of MC–ferroelectric (MC–FE) mutiferroid structures [135, 136]. The behavior of the dispersion characteristics in such a structure is determined not only by the coupling between the direct and counter magnetostatic waves in the MC resulting in the appearance of forbidden bands but also by the coupling between the MSW and an electromagnetic wave (EMW) in the FE, which depends on the electric field strength applied to the FE. In this case, the double (electric and magnetic) control of the characteristics of forbidden bands becomes possible [135, 136].

We note that the first studies of waves propagating in a layered ferromagnetic-film–ferroelectric (FM–FE) multiferroid structure were performed in the 1980s [137, 138]. For large values of the FE permittivity, which depends on the applied permanent electric field, electromagnetic waves in the FE are strongly slowed down, and in this case hybrid electromagnetic–spin waves (HEMSWs) appear in the FM–FE structure at frequencies close to the phase matching frequency for EMWs and MSWs. These structures have

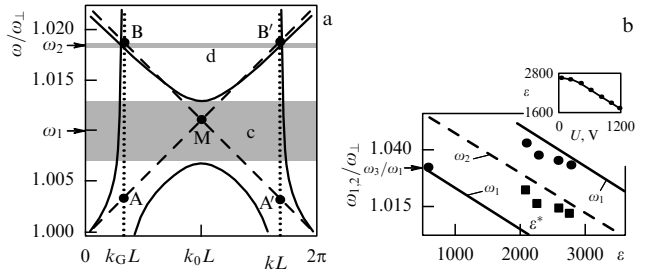

Figure 28. Calculated HEMSW characteristics in the MC–FE structure: (a) dispersion characteristics for the permittivity $\varepsilon = 1500$; (b) experimental and theoretical dependences of the central frequencies of forbidden bands on ε ($L = 200$ μm, $d/L = 0.06$, $a/L = 2.5$, $b_1/L = 0.5$, $\Delta d/L = 0.03$, $4\pi M_0 = 1825$G, $H_0 = 1080$ Oe).

recently attracted renewed interest [139–141] in connection with the development of technologies for fabricating ceramic ferroelectrics [barium titanate ($BaTiO_3$), strontium titanate ($SrTiO_3$)] with the permittivity variable in a broad range.

We note that the wave hybridization effects in FM–FE structures are presently investigated quite thoroughly upon excitation of different types of MSWs [137, 140], and the possibility of developing doubly controlled microwave devices based on them has been shown [137, 142].

The structure under study consists of a one-dimensional MC and an FE layer. The magnonic crystal is made of a ferromagnetic film with a saturation magnetization M_0 and an inhomogeneous, grooved surface. A permanent magnetic field is applied normally to the film surface. The FE layer with a permittivity ε is placed into an external electric field E.

Using the approach described in Section 2.2.1 in the linear case, we can obtain the dispersion equation for hybrid waves in the MC–FE structure [136]. Figure 28a presents solutions of the dispersion equation for direct and counter EMWs in the FE in the absence of coupling between these waves (dotted curves); for direct and counter MSWs in the MC in the absence of coupling between these waves (dashed curves); and for HEMSWs in the MC–FE structure (solid curves).

We can see that five points of intersection of these curves exist (points A, B, A′, B′, M) in which the hybridization of these types of waves can be observed. Due to hybridization of the waves at points B, B′, and M, two forbidden bands are formed (in contrast to one forbidden band in the region of the first Bragg resonance for a single MC). The first forbidden band (band c, a darker area in Fig. 28a) is formed near the point M. For the small permittivity ε, the central frequency and width of the first forbidden band coincide with those of the forbidden band of a single MC. The second forbidden band is formed near points B and B′ (band d, the darker area in Fig. 28a).

Experiments were performed using an MC made of a YIG plate with the surface covered by grooves [143]. The ferroelectric layer was a BK-8 plate with chrome electrodes deposited on both of its sides for applying a control voltage. Experimental and theoretical dependences of the central frequencies of forbidden bands on ε are compared in Fig. 28b. Circles and squares show the experimental central frequencies of respective forbidden bands c and d. The inset in Fig. 28b shows the experimental dependence of ε on the applied voltage U.

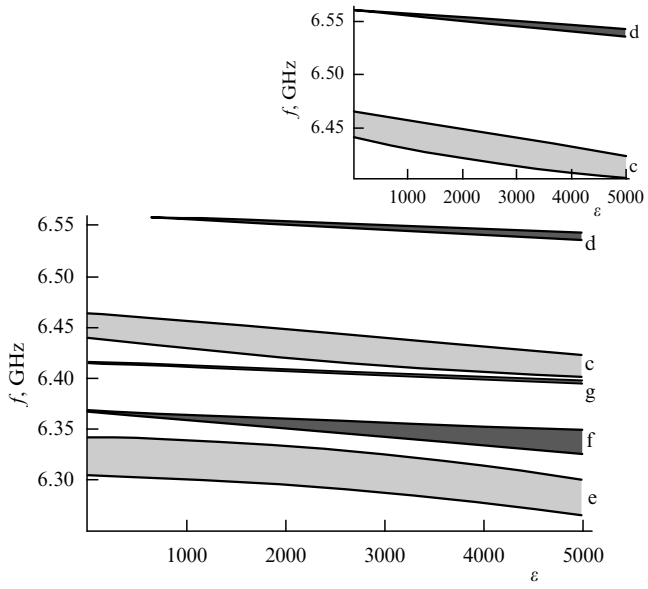

Figure 29. Dependence of the position and width of forbidden bands in the MC–FE–MC structure on ε for $H_0 = 1500$ Oe. The inset shows similar dependences in the MC–FE structure.

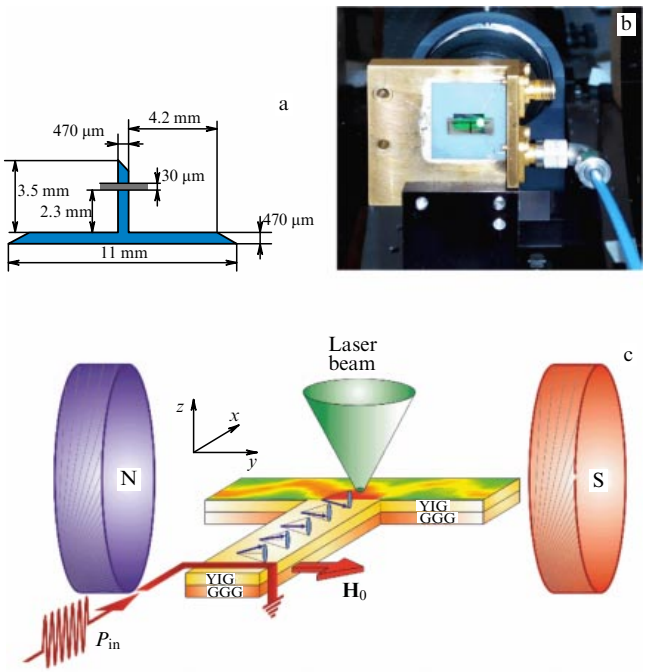

Figure 30. (a) Dimensions of a T-shaped waveguide and the location of a microstrip converter on the stem of the structure. (b) Photograph of the microstrip line structure. (c) Schematic of the MBS experiment.

It is interesting to study the structure consisting of two coupled MCs, similar to that described in Section 3.4.2 but different in that the space between the MCs is filled with an FE layer. In this case, the coupling between MCs can be electrically controlled. In the MC–FE–MC structure, five forbidden bands are formed, three of which are formed by the interaction of MSWs and EMWs and two by the interaction only between MSWs. Figure 29 shows the dependences of the width and position of all forbidden bands on the permittivity ε. We can see that for small ε, two forbidden bands c and e are formed (light regions), which are analogous to forbidden bands in a thick and thin MC, and the width of these bands is independent of ε. As ε increases at a fixed magnetic field strength, the other three forbidden bands d, f, and g appear (dark regions), with the widths increasing with increasing ε. We note that in the case of the MC–FE structure, only two forbidden bands c and d are formed (see the top of Fig. 29).

3.5.2 T-shaped power divider. Information signals are transferred in telecommunication systems through waveguides with complex configurations. For example, T-shaped optical waveguides are made in the form of a defect in a two-dimensional photonic crystal [144]. The main advantage of this structure is that it can be used as an optical switch with small radiation losses due to inhomogeneities in the propagation direction of the electromagnetic wave [145]. T-shaped structures in the form of a defect in a two-dimensional magnonic crystal were considered in [146]. However, the authors of [146] studied the propagation of electromagnetic waves in this structure only numerically. The experimental study of a T-shaped ferromagnetic waveguide was performed in [147], where a T-shaped waveguide made of a metal ferromagnetic (permalloy) was considered and the generation of backward volume spin waves in this structure was demonstrated. But because of the strong decay of spin waves in a permalloy, the use of such structures in systems for signal processing and generation seems difficult.

A T-shaped ferromagnetic waveguide was cut out from a YIG film by laser scribing. The YIG film, grown on a GGG substrate by liquid-phase epitaxy, has the thickness $d = 7.7$ μm, the saturation magnetization $4\pi M_0 = 1750$ Hz, and the ferromagnetic resonance linewidth $\Delta = 0.5$ Oe measured at the frequency of 5 GHz. The T-shaped YIG waveguide shown in Fig. 30a has the width $w = 470$ μm, the 'stem' length $l_1 = 3.5$ mm, and the 'beam' length $l_2 = 10$ mm. Magnetization waves, which are called spin waves in the literature, are excited in the YIG film by a microstrip transducer $w = 30$ μm in width with one end grounded and the other connected to a microwave oscillator. The microstrip transducer creates the antinode of an alternate microwave magnetic field, which is inhomogeneous for the YIG waveguide. For a given width of the microstrip transducer, magnetostatic spin waves are excited in the YIG film due to the long-range dipole–dipole interaction existing in the ferromagnet. The T-shaped YIG waveguide is placed between the poles of an electromagnet producing a spatially homogeneous permanent magnetic field H_0 of the strength 1160 Oe.

The space–time distribution of the magnetization **m** in the T-shaped YIG waveguide was studied with an MBS setup. The YIG film surface was scanned with a laser beam focal spot 20–30 μm in diameter (macro MBS) with the step $s_1 = 0.05$ mm in the longitudinal direction along the x axis and with the step $s_2 = 0.05$ mm in the transverse direction along the y axis (Fig. 30c). Due to inelastic light scattering by magnons, the light beam intensity I was reflected from the waveguide changes. The measured value of I is proportional to the magnetization amplitude modulus squared, $I(t, x, y) \sim |\mathbf{m}(t, x, y)|^2$. Magnetostatic waves are excited in the YIG waveguide by 500 ns microwave pulses fed to a microstrip transducer. Simultaneously, microwave pulses are fed into the MBS setup for measuring the light

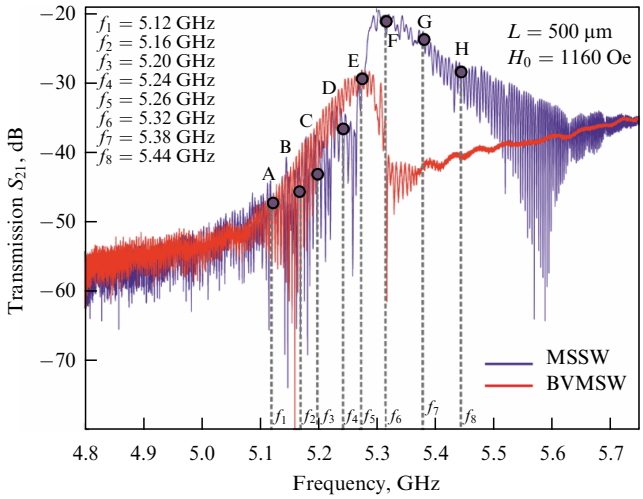

Figure 31. Amplitude–frequency characteristics of a surface and backward volume magnetostatic wave in a YIG waveguide 500 μm in width. Points A, B, C, D, E, F, G, and H indicate the input signal frequencies in MBS experiments (f_1–f_8, respectively).

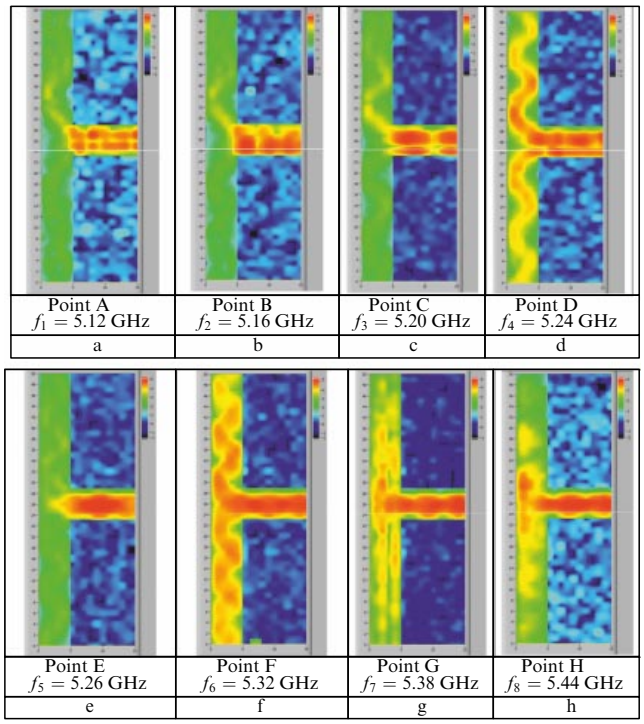

Figure 32. Spatial distributions of the magnetization amplitude squared measured in a T-shaped YIG waveguide at the frequencies indicated in Fig. 31. The vertical and horizontal sizes of the scan region are 5 and 1.5 mm, respectively. The scan resolution along each axis is 0.1 mm. In the stem of the T-shaped structure, an MSSW was excited (in the right-hand side of each image in the figure).

beam intensity. To avoid the heating of the YIG waveguide by microwave pulses, the pulse repetition period $T_r = 1.1$ μs was used. The peak power was $P_p = -30$ dBmW, which rules out the appearance of nonlinear processes in the YIG waveguide.

In the first stage, the AFCs were measured for two orientations of the external permanent magnetic field. In both cases, this field was directed tangentially to the T-shaped YIG waveguide surface. For the transverse magnetization, when $\mathbf{H}_0$ is parallel to the y axis and perpendicular to the direction of the longitudinal wave vector $\mathbf{k}_x$ of magnetization waves, a surface MSW is excited in the YIG film. For the longitudinal magnetization, when $\mathbf{H}_0 \| x \| \mathbf{k}_x$, backward volume MSWs (BVMSWs) are excited in the YIG film.

Figure 31 shows AFCs measured for the two orientations of the field $\mathbf{H}_0$. We can see that in the case of a bounded YIG waveguide, the MSSW and BVMSW frequency bands overlap in the vicinity of the frequency $f_\perp$, the upper (lower) boundary frequency of the BVMSW (MSSW) spectrum in the infinite ferromagnetic medium. The AFCs of finite-width ferrite waveguides show that the AFC spectra of surface and volume waves overlap. A similar situation also appears in a T-shaped ferrite waveguide.

To analyze these effects, T-shaped waveguides 1000 and 250 μm in width were fabricated (the results of measurements of the AFCs of these waveguides are nor presented here). It was found that a change in the width of the T-shaped YIG waveguide resulted in a change in the frequency band where the AFCs of MSSWs and BVMSWs overlapped. As the width of the T-shaped waveguide was increased, the overlap region of the spectra of these waves reduced, while a decrease in the waveguide width resulted in an increase in this region. The overlap of MSSW and BVMSW spectra is caused by the appearance of forward volume MSWs (FVMSWs) at frequencies close to $f_\perp$. The appearance of FVMSWs during the tangential magnetization is related to the restricted width of the YIG waveguide.

The existence of FVMSWs at frequencies in the region of small wave numbers of the MSSW spectrum was theoretically predicted in [121] for a finite-width YIG waveguide. The FVMSW spectrum does not disappear when the magnetic field is rotated through 90° (the case of longitudinal magnetization).

Thus, the restricted width of the YIG waveguide leads to the formation of a frequency region in the MSSW spectrum where volume waves with normal dispersion exist. We note that FVMSWs exist in the cases of transverse and longitudinal magnetizations of a bounded YIG waveguide.

Hence, due to the shape anisotropy [36] in the T-shaped structure, it is possible to control the width of the overlap frequency band for MSSWs and FVMSWs [27].

We now consider spatial distributions of the magnetization amplitude squared measured at different frequencies for a magnetic field $\mathbf{H}_0$ directed along the y axis. The input pulsed signal power was $P_{in} = 5$ dBm. The pulse duration was $\tau = 500$ ns and the pulse repetition period during the MBS scan was $T = 1000$ ns. Figure 32 shows the spatial distributions of the magnetization amplitude squared measured in the T-shaped YIG waveguide at frequencies f_1–f_8 indicated in the AFC in Fig. 31 by respective circles A, B, C, D, E, F, G, and H.

When the input signal frequency was set equal to $f_1 = 5.12$ GHz, $f_2 = 5.16$ GHz, and $f_3 = 5.20$ GHz, the signal propagated along the supply section of the T-shaped waveguide to the connection region of the waveguides. In this case, the wave did not propagate to the stems of the T-shaped waveguide behind the connection region (Figs 32a–c). This effect can be explained by the fact that the MSSW excitation efficiency at the frequencies f_1, f_2, and f_3 is rather low (as demonstrated by AFCs in Fig. 31). Therefore, although BVMSWs can be excited in this frequency region, the signal does not propagate to the stems of the T-shaped waveguide.

With the input signal frequency $f_4 = 5.24$ GHz, the signal begins to propagate along both stems of the T-shaped structure. We can see that the wave propagates from the joint site of waveguide sections over a distance not less than 2.5 mm (Fig. 32d). A detailed scan of this region in MBS experiments gave the mode composition of radiation on the input section of the T-shaped waveguide, where the superposition of the first and third modes excited by a microstrip antenna is formed. The waveguide propagation of radiation is observed in the stems of the T-shaped structure. In this case, the beating occurs between the first and second width modes of a YIG waveguide 470 μm in width [27, 28, 80–82, 121]. As the input signal frequency is increased further, a regime is observed in which the wave again does not propagate into the stems of the T-shaped waveguide (Fig. 32e). The analysis of the MSSW AFC (point E in Fig. 31) shows that the frequency $f_5 = 5.26$ GHz is in the beginning of the region of the existence of MSSWs.

When the input signal frequency is specified in the region where (for a given external permanent magnetic field) an MSSW can be excited, for example, at the frequency $f_6 = 5.32$ GHz (point F in Fig. 31), the wave branching into the stems of the T-shaped waveguide is again observed (Fig. 32f). In this case, the mode composition remains the same as at the frequency $f_4 = 5.24$ GHz. But in this case, for the input signal frequency $f_6 = 5.32$ GHz, the transverse size of the wave field increases both in the input cross section and in the stems of the T-shaped structure.

As the input signal frequency increases, the wave branching into the stems of the T-shaped waveguide ceases. When the input signal frequency is $f_7 = 5.38$ GHz (point G in Fig. 31), waveguide propagation of the wave into the stems of the structure is not observed (Fig. 32g): the wave rapidly decays during propagation into the stem of the structure. As the frequency of the excited MSSW increases, the field propagation distance in the stem of the structure decreases, as can be seen in Fig. 32h for the input signal frequency $f_8 = 5.44$ GHz.

We can see from results presented in Fig. 32 that for a strictly parallel orientation of the field $\mathbf{H}_0$ with respect to the y axis, magnetization waves propagate into both stems of the T-shaped structure. With such a field configuration, the first and third MSSW width modes are formed in the input region of the T-shaped waveguide and excite the first and second width modes in the stems of the structure [27]. It was found that when the signal frequency was higher than the intersection band of the MSSW and BVMSW, excitation of magnetization waves in both stems of the structure was not observed. In this case, in the input region of a T-shaped YIG waveguide, only the MSSW width modes were formed, which, upon reaching the plane of translation symmetry breaking, did not excite wave packets in both stems of the structure. By rotating the whole model together with the structure under study about the unchanged direction of the external permanent magnetic field, we can observe the unidirectional branching of spin waves into the stems of the T-shaped YIG waveguide. This fact opens up the possibility of using microscopic YIG waveguides in adjustable couplers and magnonic logic devices.

4. Existing devices and promising applications

The development of the physical and technological foundations of microwave data processing devices based on the propagation of spin waves in ferromagnetic films, which covers several decades, is considered in detail in reviews [148–158]. The frequency range of such devices, which is determined by the choice of the material and the magnetizing field, covers from a few tens of MHz to a few tens of GHz. The effects of propagation of spin waves are used in many low-loss (≈ 2 dB) band-transmission and band-elimination filters with filtration bands tunable to within several gigahertz [148, 150, 153–155, 158]. Sets of MSW filters were used for the development of multichannel detectors operating in the frequency range from 0.5 to 18 GHz [150].

We note that the effects of anisotropic MSW propagation can be used to fabricate spatially frequency-selective highly rectangular filters [155].

Based on spin waves, both dispersion and dispersionless spatial delay lines have been developed [148, 150, 155, 159]. We note that delay lines using hybrid magnetoelastic waves can provide delays tunable in the range from 100 ns to several microseconds [155, 156], which previously was possible only in bulk ferrite samples with a considerably inhomogeneous field distribution [160]. MSW-based delay lines can find applications in phased array antennas, pulse-compression and memory devices, and devices for separating coinciding pulses [150].

Bragg grating [149, 151] and rectangular [151] resonators have been developed, which can be used both for filtration and as frequency-specifying devices in tunable microwave oscillators. It is shown that the signal intensity can be suppressed outside the filtration band of a Bragg resonator by apodization [161].

The possibility of developing magnetooptical devices based on the diffraction of light by MSWs for applications in integrated optics is being considered [151]. Due to the strong nonlinearity of spin waves, they can be used for the construction of convolvers, frequency-selective limiters, and signal-to-noise correctors [150, 151]. Considerable effort is being devoted to the study of the possibility of using spin-wave solitons in ferrite films in information systems [162–164]. Although the developed devices are used in specialized systems and measurement techniques, they are still very far from use in mobile communication devices, which have very rapidly developed in recent decades. This is related to difficulties encountered in the matching of spin-wave devices with modern integrated technologies and to the rather large dimensions of these devices, which are a few orders of magnitude greater than those ($1.6 \times 1.2 \times 0.13$ mm) of duplex filters on surface acoustic waves [165] used in smartphones.

Modern SW devices have large dimensions, notably because in most cases they use the effects of propagation of SWs with a wavelength λ no less than a few tens or even hundreds of micrometers. Therefore, the development of physical and technological bases for spin-wave devices using nanometer SWs is of current interest. In this connection, the development of methods for the excitation and detection of submicrometer and nanometer SWs is becoming a key problem. One of the possibilities is the use of the Schlömann mechanism [167] to excite waves with the wavelength $\lambda < 1$ μm in structures with an inhomogeneous internal field [79, 156, 160].

Recently, it was shown that SWs can be excited in a region from 1 to 0.1 μm in size with the help of coplanar antennas formed by lithography directly on the surface of a submicrometer-thick ferrite film waveguide [166, 168–170]

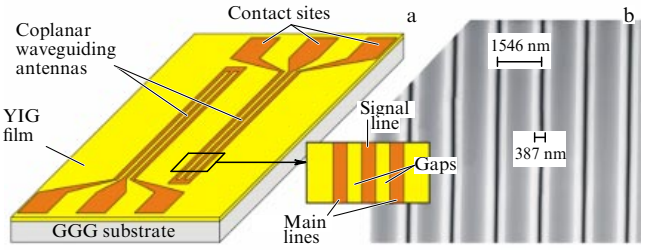

Figure 33. (a) Topology of exciting antennas formed by photolithography on the surface of a 500 nm thick epitaxial YIG film. The width of the signal and grounded conductors separated by 1.6 μm is 2 μm. (b) An image of the YIG film surface between antennas with a grating of grooves formed by ion beam etching [166].

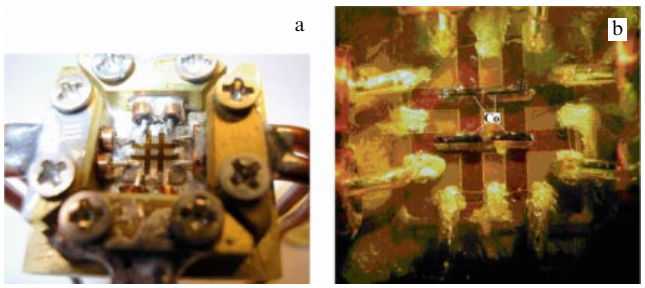

Figure 34. (a) Experimental prototype of a grating based on orthogonal YIG film waveguides with (b) cobalt microparticles in grating nodes.

(Fig. 33). The necessity of using submicrometer-thick waveguides to observe the propagation of SWs with $\lambda < 1$ μm is dictated by the dispersion properties of SWs, which lead to a drastic decrease in the group velocity in the wavelength region $\lambda < d$ [152]. We note that the use of inductive antennas for the excitation and reception of SWs in metal waveguides requires the placement of a dielectric spacer with the thickness t equal to a few tens of nanometers in thickness t between antennas and the waveguide [171–173], which restricts the wavelength of excited waves by the relation $\lambda < t$. We also note that certain progress was recently achieved in the development of methods for the deposition of YIG films not related to liquid-phase epitaxy [170, 174–178], which enhances the outlook for the development of YIG-based integrated SW devices.

The possibility of fabricating microwave modulators based on one-side metallized magnonic crystals was demonstrated in [179–185]. Such structures belong to media with broken invariance with respect to the time and coordinate transformations and can support the propagation of waves with a nonreciprocal dispersion law. Because the dispersion laws for the incident and reflected waves in an MC are different, forbidden bands appear at frequencies satisfying the generalized Bragg condition [182]. In this case, depending on the dielectric gap between the metal and MC and structure parameters, the suppression [179–181] and shift [183, 184] of forbidden-band frequencies can be observed in the MC, which can be used to control microwave signal parameters [185].

The possibility of creating magnetic logic [186–199] and memory [199–202] devices based on the interference of spin waves has been actively studied in recent years. The main constructive elements in the development of logic elements are Mach–Zehnder interferometers [186–192], in which the result of interference between SWs at the output is determined by the difference in the phase incursions of SWs propagating in each arm of the interferometer. The SW phase can be controlled by different mechanisms, such as a nonlinear phase shift at powers exceeding the parametric instability threshold [186, 187], a change in the waveguide magnetizing field [188–190], local variation of the anisotropy field [191], or the scattering of SWs by domain walls [192]. The output-signal phase and amplitude can also be controlled by changing the interaction of SWs with nanoresonators located near the waveguide surface [193] or by using waves with the nonreciprocal dispersion in the interferometer arms [194].

The authors of [195] considered the possibility of constructing logic elements based on a system of orthogonal waveguides, the output signal being determined by the interference of signals in the waveguide intersection region.

We note that the architecture of magnonic processors was discussed in [196–198]. It is pointed out that they can be developed only using nanometer SWs excited and received with the help of magnetoelectric nanostructures located on the waveguide surface (also used for data recording).

Another promising area to use nanometer SWs is magnonic holographic memory [199–201]. The author of [199] proposed the concept of such memory based on the dependence of the result of interference of SWs at the outputs of an array of orthogonal waveguides on the input phase and the magnetization of magnetic nanostructures located in the waveguide intersection nodes. Prototypes in the form of 6- and 8-port (Fig. 34) arrays of orthogonal film YIG waveguides studied in [200–202] showed the relation of output signal amplitudes to the orientation of cobalt microparticles in the array nodes. It was shown that the output signal level depended on the input signal phase and the orientation of cobalt particles.

Obviously, to construct such magnonic networks, it is necessary to solve many technological and physical problems. First of all, it is necessary to choose appropriate materials and technologies for the development of such branched nanometer SW waveguides with low microwave losses. It is also necessary to study the propagation features of SWs in waveguide arrays due to waveguide bends and turns [203–206], the strong inhomogeneity of the ground state due to the influence of demagnetization fields, which leads to the enrichment of the SW spectrum [104, 207, 298], and mode conversion effects [81]. Also, effects related to the spectrum quantization over the waveguide width [121] and the anisotropy of dispersion characteristics of SWs [209], which require a separate consideration for nanometer SWs [210–212], should be investigated.

5. Conclusions

A new direction in magnetism, in particular, in magnetic spintronics, so-called magnonics, has been rapidly developed in the last few years. Magnonics actually studies phenomena related to the dynamics of magnetic excitation quanta, magnons, in thin magnetic layers and multilayer micro- and nanostructures.

This paper is devoted to a systematic description of recent papers in the field of magnonics. We have discussed in detail theoretical and experimental methods used for studying wave phenomena related to the propagation of spin waves (magnons) in magnetic films, heterostructures, and micro- and nanosamples. One of the most efficient experimental

methods is Mandelshtam–Brillouin spectroscopy with submicron spatial resolution. In addition, spectroscopic methods involving the excitation of spin waves by microstrip converters and their propagation in coplanar lines have been efficiently used. The propagation, reflection, and scattering of magnons by magnetic micro- and nanostructures are efficiently described by semianalytic methods, such as the coupled-wave method, the multiple-scattering method, and numerical methods.

We have presented the results of studies of numerous magnetic micro-, nano-, and heterostructures, such as distributed periodic systems, lumped systems, irregular and coupled waveguide systems, and controllable magnetic structures. Aside from the description of many physical phenomena involved in the study of such structures, numerous particular devices for data processing and storage in the microwave range have been proposed. The outlook for further studies of these structures have been discussed and their applications in spintronic devices have been considered.

Acknowledgments

The work was supported by the Russian Science Foundation (grant no. 14-19-00760), the Russian Foundation for Basic Research (grant nos. 15-07-08152A, 15-07-05901, 14-07-00896-a, 13-07-00941-a, 14-07-90001-Bel_a, 13-0712421-ofi-m, 14-02-00577, 13-07-12409, 15-37-51253, 14-07-00273, 14-02-00577, 14-02-00976), the Belarus Republic Foundation for Basic Research (F14P-017), and the RF President scholarship no. 313.2015.5.

References

1. Chumak A V et al. *Nature Phys.* **11** 453 (2015)
2. Kruglyak V V, Demokritov S O, Grundler D *J. Phys. D Appl. Phys.* **43** 264001 (2010)
3. Krawczyk M, Grundler D *J. Phys. Condens. Matter* **26** 123202 (2014)
4. Wolf S A et al. *Science* **294** 1488 (2001)
5. Žutić I, Fuhrer M *Nature Phys.* **1** 85 (2005)
6. Neusser S, Grundler D *Adv. Mater.* **21** 2927 (2009)
7. Lenk B et al. *Phys. Rep.* **507** 107 (2011)
8. Pulizzi F *Nature Mater.* **11** 367 (2012)
9. Stamps R L et al. *J. Phys. D Appl. Phys.* **47** 333001 (2014)
10. Mandelstam L I *Zh. Russk. Fiz.-Khim. Obshch. Ch. Fiz.* **58** 381 (1926); *Polnoe Sobranie Trudov* (Complete Collection of Works) Vol. 1 (Moscow: Izd. Akad. Nauk SSSR, 1948) p. 280
11. Brillouin L *Ann. Physique* **17** 88 (1922)
12. Borovik-Romanov A S, Kreines N M, Zhotikov V G *Sov. Phys. Usp.* **21** 538 (1978); *Usp. Fiz. Nauk* **125** 355 (1978)
13. Camley R E, Mills D L *J. Appl. Phys.* **50** 7779 (1979)
14. Rojdestvenski I V, Cottam M G, Slavin A N *J. Appl. Phys.* **73** 7001 (1993)
15. Demokritov S O, Hillebrands B, Slavin A N *Phys. Rep.* **348** 441 (2001)
16. Cottam M G, Lockwood D J *Light Scattering in Magnetic Solids* (New York: Wiley, 1986)
17. Patton C E *Phys. Rep.* **103** 251 (1984)
18. Griffin A *Rev. Mod. Phys.* **40** 167 (1968)
19. Chu P, Mills D L *Phys. Rev. B* **75** 054405 (2007)
20. Stashkevich A A et al. *J. Magn. Magn. Mater.* **321** 876 (2009)
21. Forrest J A, Dalnoki-Veress K, Dutcher J R *Phys. Rev. E* **58** 6109 (1998)
22. Voronin D V et al. *Tech. Phys. Lett.* **39** 715 (2013); *Pis'ma Zh. Tekh. Fiz.* **39** (16) 6 (2013)
23. Belmeguenai M et al. *Phys. Rev. B* **79** 024419 (2009)
24. Büttner O et al. *Phys. Rev. B* **61** 11576 (2000)
25. Romanenko D V et al. *IEEE Trans. Magn.* **50** 4006304 (2014)
26. Serga A A, Chumak A V, Hillebrands B *J. Phys. D Appl. Phys.* **43** 264002 (2010)
27. Sadovnikov A V et al. *Appl. Phys. Lett.* **106** 192406 (2015)
28. Beginin E N, Sadovnikov A V, Sharaevsky Yu P, Nikitov S A *Solid State Phenomena* **215** 389 (2014)
29. Sheshukova S E et al. *IEEE Magn. Lett.* **5** 1 (2014)
30. Žutić I, Fabian J, Das Sarma S *Rev. Mod. Phys.* **76** 323 (2004)
31. Demidov V E et al. *Sci. Rep.* **5** 8578 (2015)
32. Demidov V E et al. *Appl. Phys. Lett.* **105** 172410 (2014)
33. Demidov V E et al. *Appl. Phys. Lett.* **106** 022403 (2015)
34. Sandercock J R, Wettling W *J. Appl. Phys.* **50** 7784 (1979)
35. Stancil D D, Prabhakar A *Spin Waves: Theory and Applications* (New York: Springer, 2009)
36. Gurevich A G, Melkov G A *Magnetization Oscillations and Waves* (New York: CRC Press, 1996)
37. Vashkovskii A V, Stal'makhov V S, Sharaevskii Yu P *Magnitostaticheskie Volny v Elektronike Sverkhvysokikh Chastot* (Magnetostatic Waves in Microwave Electronics) (Saratov: Izd. Saratovskogo Univ., 1993)
38. Marcuse D *Light Transmission Optics* (New York: Van Nostrand Reinhold, 1972); Translated into Russian: *Opticheskie Volnovody* (Optical Fibers) (Moscow: Mir, 1974)
39. Brillouin L, Parodi M *Propagation des ondes dans les Milieux Périodiques* (Paris: Masson-Dunod, 1956); Translated into Russian: *Rasprostranenie Voln v Periodicheskikh Strukturakh* (Propagation of Waves in Periodic Structures) (Moscow: IL, 1959)
40. Kivshar Yu S, Agrawal G P *Optical Solitons: From Fibers to Photonic Crystals* (Amsterdam: Academic Press, 2003); Translated into Russian: *Opticheskie Solitony. Ot Svetovodov do Fotonnykh Kristallov* (Moscow: Fizmatlit, 2005)
41. Morozova M A, Sheshukova S E, Sharaevskii Yu P *Izv. Vyssh. Uchebn. Zaved. Prikl. Nelin. Dinamika* **18** (5) 113 (2010)
42. Barabanenkov Yu, Osokin S, Kalyabin D, Nikitov S *Phys. Rev. B* **91** 214419 (2015)
43. Lisenkov I, Kalyabin D, Nikitov S *Appl. Phys. Lett.* **103** 202402 (2013)
44. Stratton J A *Electromagnetic Theory* (New York: McGraw-Hill, 1941)
45. Zienkiewicz O C, Morgan K *Finite Elements and Approximation* (New York: Wiley, 1983); Translated into Russian: *Konechnye Elementy i Approksimatsiya* (Moscow: Mir, 1986)
46. Silvester P P, Ferrari R L *Finite Elements for Electrical Engineers* 3rd ed. (New York: Cambridge Univ. Press, 1996)
47. Sadovnikov A V, Rozhnev A G *Izv. Vyssh. Uchebn. Zaved. Prikl. Nelin. Dinamika* **20** (1) 143 (2012)
48. Vasil'ev I V, Kovalev S I *Radiotekh. Elektron.* **38** 2174 (1993)
49. Vasil'ev I V, Kovalev S I *IEEE Trans. Microwave Theory Tech.* **42** 1238 (1994)
50. Long Y, Koshiba M, Suzuki M *IEEE Trans. Microwave Theory Tech.* **35** 731 (1987)
51. Sadovnikov A V et al. *J. Commun. Technol. Electron.* **59** 914 (2014); *Radiotekh. Elektron.* **59** 876 (2014)
52. Taflove A, Hagness S C *Computational Electrodynamics: The Finite-Difference Time-Domain Method* (Boston, MA: Artech House, 2005)
53. Donahue M J, Porter D G "Oommf user's guide, version 1.0", NIST Interagency/Internal Report (NISTIR) 6376 (Gaithersburg, MD: NIST, 1999)
54. Vansteenkiste A, Van de Wiele B *J. Magn. Magn. Mater.* **323** 2585 (2011)
55. Vansteenkiste A et al. *AIP Adv.* **4** 107133 (2014)
56. Kumar D et al. *J. Phys. D Appl. Phys.* **45** 015001 (2012)
57. Kim S-K *J. Phys. D Appl. Phys.* **43** 264004 (2010)
58. Guslienko K Yu, Slavin A N *Phys. Rev. B* **72** 014463 (2005)
59. Ustinov A B et al. *Phys. Rev. B* **81** 180406 (2010)
60. Akhmediev N N, Ankiewicz A *Solitons: Nonlinear Pulses and Beams* (London: Chapman and Hall, 1997); Translated into Russian: *Solitony. Nelineinye Impul'sy i Puchki* (Moscow: Fizmatlit, 2003)
61. Morozova M A, Nikitov S A, Sharaevskii Yu P, Sheshukova S E *Acta Phys. Polon. A* **121** 1173 (2012)
62. Sheshukova S E et al. *Phys. Wave Phenom.* **21** 304 (2013)
63. Sheshukova S E et al. *Solid State Phenom.* **215** 394 (2014)
64. Kruglyak V V et al. *J. Appl. Phys.* **99** 08C906 (2006)
65. Yang H, Yun G, Cao Y *J. Appl. Phys.* **112** 103911 (2012)

66. Kuchko A N, Sokolovskii M L, Kruglyak V V *Physica B* **370** 73 (2005)
67. Filimonov Y, Pavlov E, Vystostkii S, Nikitov S *Appl. Phys. Lett.* **101** 242408 (2012)
68. Chi K H, Zhu Y, Tsai C S *J. Appl. Phys.* **115** 17D125 (2014)
69. Schwarze T, Grundler D *Appl. Phys. Lett.* **102** 222412 (2013)
70. Gulyaev Yu V et al. *JETP Lett.* **77** 567 (2003); *Pis'ma Zh. Eksp. Teor. Fiz.* **77** 670 (2003)
71. Obry B et al. *Appl. Phys. Lett.* **102** 202403 (2013); *Appl. Phys. Lett.* **102** 022409 (2013)
72. Nikitov S A, Tailhades Ph, Tsai C S *J. Magn. Magn. Mater.* **236** 320 (2001)
73. Chumak A V et al. *Appl. Phys. Lett.* **95** 262508 (2009)
74. Arikan M et al. *J. Phys. D Appl. Phys.* **46** 135003 (2013)
75. Chumak A V et al. *J. Phys. D Appl. Phys.* **42** 205005 (2009)
76. Chumak A V et al. *Appl. Phys. Lett.* **95** 262508 (2009)
77. Ciubotaru F et al. *J. Phys. D Appl. Phys.* **45** 255002 (2012)
78. Lee K-S, Han D-S, Kim S-K *Phys. Rev. Lett.* **102** 127202 (2009)
79. Demidov V E et al. *Appl. Phys. Lett.* **99** 172501 (2011)
80. Beginin E N et al. *Bull. Russ. Acad. Sci. Phys.* **77** 1429 (2013); *Izv. Ross. Akad. Nauk Ser. Fiz.* **77** 1735 (2013)
81. Demidov V E et al. *Phys. Rev. B* **79** 054417 (2009)
82. Demidov V E et al. *Phys. Rev. B* **77** 064406 (2008)
83. Wolf W P, Rodrigue G P *J. Appl. Phys.* **29** 105 (1958)
84. Cherepanov V, Kolokolov I, L'vov V *Phys. Rep.* **229** 81 (1993)
85. Ignatchenko V A, Mankov Yu I, Maradudin A A *Phys. Rev. B* **59** 42 (1999)
86. Kruglyak V V, Kuchko A N *Physica B* **339** 130 (2003)
87. Kruglyak V V, Kuchko A N *J. Magn. Magn. Mater.* **272–276** 302 (2004); in *Proc. of the Intern. Conf. on Magnetism* (*ICM 2003*) *Rome, Italy, 27 July – 1 August 2003*
88. Tkachenko V S, Kruglyak V V, Kuchko A N *J. Magn. Magn. Mater.* **307** 48 (2006)
89. Ignatchenko V A, Mankov Yu I, Maradudin A A *Phys. Rev. B* **62** 2181 (2000)
90. Gulyaev Yu V, Nikitov S A *Dokl. Phys.* **46** 687 (2001); *Dokl. Ross. Akad. Nauk* **380** 469 (2001)
91. Kuchko A N, Sokolovskii M L, Kruglyak V V *Phys. Met. Metallogr.* **101** 513 (2006); *Fiz. Met. Metalloved.* **101** 565 (2006)
92. Filimonov Yu A, Nikitov S A, Pavlov E S, Vysotsky S L, in *Nanostructures: Physics and Technology. Proc. of the 20th Intern. Symp., Nizhny Novgorod, Russia, June 24 – 30, 2012* (St. Petersburg: Academic Univ. Publ., 2012) p. 43
93. Pavlov E S, Filimonov Yu A, in *Intern. Symp. Spin Waves, St. Petersburg, Russia, June 7 – 13 2015, Abstracts* (St. Petersburg: Ioffe Physical-Technical Institute, 2015) p. 122
94. Gulyaev Yu V, Nikitov S A, Plesskii V P *Radiotekh. Elektron.* **26** 2282 (1981)
95. Pavlov E S, Filimonov Yu A *Nelin. Mir* (2) 35 (2015)
96. Vysotskii S L et al. *Izv. Vyssh. Uchebn. Zaved. Prikl. Nelin. Dinamika* **20** (2) 3 (2012)
97. Schneider C M, in *Spintronics — from GMR to Quantum Information: Lecture Notes of the 40th IFF Spring School, March 9 – 20, 2009, Jülich, Germany* (Eds St Blügel et al.) (Jülich: Forschungszentrum Jülich GmbH, 2009)
98. Žutić I, Fuhrer M *Nature Phys.* **1** 85 (2005)
99. Morris D H et al. *Int. J. High Speed Electron. Syst.* **21** 1250005 (2012)
100. Kruglyak V V et al. *Phys. Rev. Lett.* **104** 027201 (2010)
101. Ding J, Adeyeye A O *Appl. Phys. Lett.* **101** 103117 (2012)
102. Gulyaev Yu V et al. *JETP Lett.* **77** 567 (2003); *Pis'ma Zh. Eksp. Teor. Fiz.* **77** 670 (2003)
103. Vysotskii S L, Nikitov S A, Filimonov Yu A *JETP* **101** 547 (2005); *Zh. Eksp. Teor. Fiz.* **128** 636 (2005)
104. Jorzick J et al. *Phys. Rev. Lett.* **88** 047204 (2002)
105. Gubbiotti G et al. *J. Phys. Condens. Matter* **16** 7709 (2004)
106. Ciubotaru F et al. *Phys. Rev. B* **88** 134406 (2013)
107. Guslienko K Yu, Slavin A N *J. Appl. Phys.* **87** 6337 (2000)
108. Krawczyk M et al. *J. Phys. D Appl. Phys.* **46** 495003 (2013)
109. Zivieri R et al. *Phys. Rev. B* **85** 012403 (2012)
110. Chi K H, Zhu Y, Tsai C S *IEEE Trans. Magn.* **49** 1000 (2013)
111. Neusser S, Botters B, Grundler D *Phys. Rev. B* **78** 054406 (2008)
112. Neusser S et al. *Appl. Phys. Lett.* **93** 122501 (2008)
113. Neusser S et al. *Phys. Rev. B* **84** 094454 (2011)
114. Shindou R et al. *Phys. Rev. B* **87** 174402 (2013)
115. Shindou R, Ohe J *Phys. Rev. B* **89** 054412 (2014)
116. Lisenkov I et al. *Phys. Rev. B* **90** 104417 (2014)
117. Shindou R et al. *Phys. Rev. B* **87** 174427 (2013)
118. Sebastian T et al. *Phys. Rev. Lett.* **110** 067201 (2013)
119. Mathieu Ch, Synogatch V T, Patton C E *Phys. Rev. B* **67** 104402 (2003)
120. Ordóñez-Romero C L et al. *Phys. Rev. B* **79** 144428 (2009)
121. O'Keeffe T W, Patterson R W *J. Appl. Phys.* **49** 4886 (1978)
122. Bajpai S N *J. Appl. Phys.* **58** 910 (1985)
123. Joseph R I, Schlömann E *J. Appl. Phys.* **36** 1579 (1965)
124. Fjerstad R L *IEEE Trans. Microwave Theory Tech.* **18** 205 (1970)
125. Helszajn J *Microwave J.* **21** 53 (1978)
126. Sasaki H, Mikoshiba N *J. Appl. Phys.* **52** 3546 (1981)
127. Annenkov A Yu, Gerus S V, Kovalev S I *Tech. Phys.* **43** 216 (1998); *Zh. Tekh. Fiz.* **68** (2) 91 (1998)
128. Kim S-K, Lee K-S, Han D-S *Appl. Phys. Lett.* **95** 082507 (2009)
129. Grishin S V et al. *J. Appl. Phys.* **115** 053908 (2014)
130. Morozova M A et al. *IEEE Trans. Magn.* **50** 4007204 (2014)
131. Morozova M A, Matveev O V *Phys. Wave Phenom.* **23** 114 (2015)
132. Beginin E N, Morozova M A, Sharaevskii Yu P *Phys. Solid State* **52** 79 (2010); *Fiz. Tverd. Tela* **52** 76 (2010)
133. Sharaevskii Yu P, Grishin S V, Malyugina M A *Izv. Vyssh. Uchebn. Zaved. Prikl. Nelin. Dinamika* **14** (8) 45 (2006)
134. Morozova M A et al. *Phys. Solid State* **54** 1575 (2012); *Fiz. Tverd. Tela* **54** 1478 (2012)
135. Ustinov A B, Kalinikos B A *Tech. Phys. Lett.* **40** 568 (2014); *Pis'ma Zh. Tekh. Fiz.* **40** (13) 58 (2014)
136. Morozova M A, Sharaevskii Yu P, Nikitov S A *J. Commun. Technol. Electron.* **59** 467 (2014); *Radiotekh. Elektron.* **59** 510 (2014)
137. Anfinogenov V B et al. *Sov. Tech. Phys. Lett.* **12** 389 (1986); *Pis'ma Zh. Tekh. Fiz.* **12** 938 (1986)
138. Gulyaev Yu V, Zil'berman P E *Spinvolnovaya Elektronika* (Spin-Wave Electronics) (News in Life, Science, and Technology. Radio Engineering and Communication, Issue 9, 1988) (Moscow: Znanie, 1988)
139. Demidov V E, Kalinikos B A, Edenhofer P *Tech. Phys.* **47** 343 (2002); *Zh. Tekh. Fiz.* **72** (3) 61 (2002)
140. Ustinov A B, Srinivasan G, Kalinikos B A *Appl. Phys. Lett.* **90** 031913 (2007)
141. Nikitin A A et al., in *Proc. of the 42nd European Microwave Conf., Amsterdam, Netherlands, 29 October – 01 November 2012*, p. 783
142. Ustinov A B et al. *J. Appl. Phys.* **100** 093905 (2006)
143. Morozova M et al. *IEEE Trans. Magn.* **PP** (99) 1 (2015)
144. Fan S et al. *J. Opt. Soc. Am. B* **18** 162 (2001)
145. Djavid M et al. *Physica E* **40** 3151 (2008)
146. He C et al. *Appl. Phys. Lett.* **96** 111111 (2010)
147. Brächer T et al. *Appl. Phys. Lett.* **102** 132411 (2013)
148. Vapne G M *Obzory Elektron. Tekh. Ser. 1 Elektronika SVCh* (8) 1060 (1984)
149. Reed K W, Owens J M, Carter R L *Circuits Syst. Signal Proces.* **4** (1 – 2) 157 (1985)
150. Adam J D *Proc. IEEE* **76** 159 (1988); *TIIER* **76** (2) 73 (1988)
151. Ishak W S *Proc. IEEE* **76** 171 (1988); *TIIER* **76** (2) 86 (1988)
152. Morgentaler F R *Proc. IEEE* **76** (2) 138 (1988); *TIIER* **76** (2) 324 (1988)
153. Vendik O G, Kalinikos B A (Eds) "Fizika spinvolnovykh protsessov v ferromagnitnykh plenkakh i sloistykh strukturakh" ("Physics of spin-wave processes in ferromagnetic films and layered structures") *Izv. Vyssh. Uchebn. Zaved. Fiz.* **31** (11) 124 (1988), thematic issue
154. Vashkovsky A V, Lokk E H *Phys. Usp.* **49** 537 (2006); *Usp. Fiz. Nauk* **176** 557 (2006)
155. Anfinogenov V B et al. *Radiotekh.* (8) 6 (2000)
156. Zil'berman P E, Temiryazev A G, Tikhomirova M P *Phys. Usp.* **38** 1173 (1995); *Usp. Fiz. Nauk* **165** 1219 (1995)
157. Adam J D et al. *IEEE Trans. Microwave Theory Tech.* **50** 721 (2002)
158. Uher J, Hoefer W J R *IEEE Trans. Microwave Theory Tech.* **39** 643 (1991)
159. Vysotskii S L et al. *Tech. Phys. Lett.* **32** 667 (2006); *Pis'ma Zh. Tekh. Fiz.* **32** (15) 45 (2006)
160. Eshbach J R *J. Appl. Phys.* **34** 1298 (1963)
161. Maeda A, Susaki M *IEEE Trans. Magn.* **42** 3096 (2006)

162. Kalinikos B A, Kovshikov N G, Slavin A N *JETP Lett*. **38** 413 (1983); *Pis'ma Zh. Eksp. Teor. Fiz*. **38** 343 (1983)
163. Kalinikos B A, Kovshikov N G, Patton C E *Phys. Rev. Lett*. **80** 4301 (1998)
164. Marcelli R et al. *IEEE Trans. Magn*. **42** 1785 (2006)
165. Bauer T et al. *IEEE Microwave Mag*. **16** (7) 73 (2015)
166. Khivintsev Y et al., in *IEEE Intern. Magnetics Conf. INTERMAG Europe 2014, Dresden, Germany, May 4–8 2014, Digest Book*, p. 1120
167. Singer J R (Ed.) *Advances in Quantum Electronics* (New York: Columbia Univ. Press, 1961)
168. Khivintsev Y V et al., in *Intern. Symp. on Spin Waves 2013, St. Petersburg, Russia, June 9–15, 2013, Abstracts Book* (St. Petersburg: Ioffe Physical-Technical Institute, 2013) p. 67
169. Khivintsev Y V, Filimonov Y A, Nikitov S A *Appl. Phys. Lett*. **106** 052407 (2015)
170. Haiming Yu et al. *Sci. Rep*. **4** 6848 (2014)
171. Fallarino L et al. *IEEE Trans. Magn*. **49** 1033 (2013)
172. Huber R et al. *Appl. Phys. Lett*. **102** 012403 (2013)
173. Chang C S et al. *Appl. Phys. Lett*. **104** 032408 (2014)
174. Manuilov S A et al. *J. Appl. Phys*. **105** 033917 (2009)
175. Stognij A I et al. *J. Appl. Phys*. **118** 023905 (2015)
176. Boudiar T et al. *Phys. Status Solidi C* **1** 3347 (2004)
177. Yamamoto S et al. *Phys. Status Solidi A* **201** 1810 (2004)
178. Sun Y et al. *Appl. Phys. Lett*. **101** 152405 (2012)
179. Vysotskii S L et al. *Tech. Phys. Lett*. **37** 1024 (2011); *Pis'ma Zh. Tekh. Fiz*. **37** (21) 76 (2011)
180. Beginin E N et al. *Appl. Phys. Lett*. **100** 252412 (2012)
181. Vysotskii S L et al. *J. Commun. Technol. Electron*. **58** 347 (2013); *Radiotekh. Elektron*. **58** 389 (2013)
182. Mruczkiewicz M et al. *New J. Phys*. **15** 113023 (2013)
183. Mruczkiewicz M et al. *IEEE Trans. Magn*. **50** (11) 2304103 (2014)
184. Mruczkiewicz M et al. *Phys. Rev. B* **90** 174416 (2014)
185. Nikitov S A et al., Patent RF 2454788 (2012)
186. Fetisov Y K, Patton C E *IEEE Trans. Magn*. **35** 1024 (1999)
187. Ustinov A B, Kalinikos B A *Tech. Phys. Lett*. **27** 403 (2001); *Pis'ma Zh. Tekh. Fiz*. **27** (10) 20 (2001)
188. Kostylev M P et al. *Appl. Phys. Lett*. **87** 153501 (2005)
189. Schneider T et al. *Appl. Phys. Lett*. **92** 022505 (2008)
190. Lee K-S, Kim S-K *J. Appl. Phys*. **104** 053909 (2008)
191. Vasiliev S V et al. *J. Appl. Phys*. **101** 113919 (2007)
192. Hertel R, Wulfhekel W, Kirschner J *Phys. Rev. Lett*. **93** 257202 (2004)
193. Au Y et al. *Appl. Phys. Lett*. **100** 172408 (2012)
194. Jamali M et al. *Sci. Rep*. **3** 3160 (2013)
195. Nanayakkara K et al. *IEEE Trans. Magn*. **50** (11) 3402204 (2014)
196. Khitun A, Wang K L *Superlat. Microstruct*. **37** 55 (2005)
197. Khitun A, Wang K L *J. Appl. Phys*. **110** 034306 (2011)
198. Khitun A *J. Appl. Phys*. **111** 054307 (2012)
199. Khitun A *J. Appl. Phys*. **113** 164503 (2013)
200. Gertz F et al. *IEEE Trans. Magn*. **51** 4002905 (2015)
201. Kozhevnikov A et al. *Appl. Phys. Lett*. **106** 142409 (2015)
202. Kozhevnikov A et al., in *Spin Waves 2015 Intern. Symp. SW2015, St. Petersburg, Russia, June 7–13, 2015, Abstracts* (2015) p. 75
203. Clausen P et al. *Appl. Phys. Lett*. **99** 162505 (2011)
204. Vogt K et al. *Appl. Phys. Lett*. **101** 042410 (2012)
205. Tkachenko V S et al. *Appl. Phys. Lett*. **101** 152402 (2012)
206. Xing X et al. *Sci. Rep*. **3** 2958 (2013)
207. Bayer C et al. *Phys. Rev. B* **69** 134401 (2004)
208. Vysotskii S L et al. *JETP Lett*. **88** 461 (2008); *Pis'ma Zh. Eksp. Teor. Fiz*. **88** 534 (2008)
209. Grechushkin K V, Stal'makhov A V, Tyulyukin V A *Pis'ma Zh. Tekh. Fiz*. **14** 1973 (1988)
210. Pirro Ph et al. *Phys. Status Solidi B* **248** 2404 (2011)
211. Demidov V E et al. *J. Appl. Phys*. **97** 10A717 (2005)
212. Demidov V E et al. *Phys. Rev. B* **80** 014429 (2009)